

# Complex Variability of the $H\alpha$ Emission Line Profile of the T Tauri Binary System KH 15D: The Influence of Orbital Phase, Occultation by the Circumbinary Disk, and Accretion Phenomenae

Catrina M. Hamilton

*Department of Physics and Astronomy, Dickinson College, Carlisle, PA 17013*

hamiltoc@dickinson.edu

Christopher M. Johns-Krull

*Department of Physics and Astronomy, Rice University, Houston, TX 77005*

cmj@rice.edu

Reinhard Mundt

*Max-Planck-Institut für Astronomie, Königstuhl 17, D-69117 Heidelberg, Germany*

mundt@mpia.de

William Herbst

*Astronomy Department, Wesleyan University, Middletown, CT 06459*

wherbst@wesleyan.edu

Joshua N. Winn

*Department of Physics, Massachusetts Institute of Technology, Cambridge, MA 02139*

jwinn@mit.edu

## ABSTRACT

We have obtained 48 high resolution echelle spectra of the pre-main sequence eclipsing binary system KH 15D (V582 Mon,  $P = 48.37$  d,  $e \sim 0.6$ ,  $M_A = 0.6 M_\odot$ ,  $M_B = 0.7 M_\odot$ ). The eclipses are caused by a circumbinary disk seen nearly edge on, which at the epoch of these observations completely obscured the orbit of star B and a large portion of the orbit of star A. The spectra were obtained

over five contiguous observing seasons from 2001/2002 to 2005/2006 while star A was fully visible, fully occulted, and during several ingress and egress events. The  $H\alpha$  line profile shows dramatic changes in these time series data over timescales ranging from days to years. A fraction of the variations are due to “edge effects” and depend only on the height of star A above or below the razor sharp edge of the occulting disk. Other observed variations depend on the orbital phase: the  $H\alpha$  emission line profile changes from an inverse P Cygni type profile during ingress to an enhanced double-peaked profile, with both a blue and red emission component, during egress. Each of these interpreted variations are complicated by the fact that there is also a chaotic, irregular component present in these profiles. We find that the complex data set can be largely understood in the context of accretion onto the stars from a circumbinary disk with gas flows as predicted by the models of eccentric T Tauri binaries put forward by Artymowicz & Lubow, Günther & Kley, and de Val-Borro et al. In particular, our data provide strong support for the pulsed accretion phenomenon, in which enhanced accretion occurs during and after perihelion passage.

*Subject headings:* stars:individual (KH 15D) — spectroscopy — accretion — binaries

DRAFT VERSION: March 2, 2013

## 1. Introduction

KH 15D, first observed at Van Vleck Observatory in 1995, gained its notoriety due to the regular and rather large amplitude variability it displayed (Kearns & Herbst 1998). At that time, the system’s light was observed to diminish by nearly 3 magnitudes every 48.4 days, and remain in this diminished or eclipsed state for approximately 16 days, with an unusual return to near-normal brightness close to mid-eclipse. By 2000, the central reversal in the light curve had faded and the length of time that the star spent in the eclipsed state had grown slightly ( $\sim 1$  day). Spectra taken of the object in and out of eclipse had shown that there was effectively no color change between states, implying that the source of obscuration was either an optically thick disk or rather large particles (Hamilton et al. 2001). Several models were proposed at this time (Herbst et al. 2002; Barge & Viton 2003; Agol et al. 2004) that involved some sort of warp or swarm of particles in a circumstellar disk around a single star.

KH 15D was also discovered to be the source of a bipolar jet revealed in  $H\alpha$  and [OI] (Hamilton et al. 2003) whose possible launching mechanism has been discussed in detail by Mundt et al. (2010). The system is associated with a shocked  $H_2$  emission filament (Deming, Charbonneau, & Harrington 2004; Tokunaga et al. 2004). During eclipse, the spectrum of KH 15D often exhibits extended wings of  $H\alpha$  emission, up to several hundreds of  $\text{km s}^{-1}$ , characteristic of actively accreting classical T Tauri stars (CTTSs). Out of eclipse, the EW of  $H\alpha$  is only a few angstroms, which would normally lead to a classification as a weak-lined T Tauri star (WTTS) (Hamilton et al. 2003). It is perhaps best described as a weakly accreting T Tauri star. Its age, estimated from membership in NGC 2264, is  $\sim 3$  Myr.

In 2004, it was discovered that KH 15D is a binary system. Johnson et al. (2004) conducted a radial velocity survey of the system over the course of two observing seasons (2002/2003 and 2003/2004) during which KH 15D underwent significant radial velocity variations consistent with a binary companion with an orbital period equal to that of the photometric period of 48 days. Almost simultaneously, two models were put forward to explain the changing light curve as the result of the progressive occultation of a pre-main sequence binary orbit by a precessing circumbinary inner disk or ring (Winn et al. 2004; Chiang & Murray-Clay 2004). This type of model had the advantage of also being consistent with the historical light curves obtained from a study of archival photographic plates (Winn et al. 2003; Johnson & Winn 2004). Winn et al. (2006; hereafter W06) further refined this model by including a wealth of additional photometric data available from the literature (Johnson et al. 2005; Maffei et al. 2005; Hamilton et al. 2005; Barsunova et al. 2005; Kusakabe et al. 2005).

Our current working model of the system (W06) has the distinguishing aspect that the system is fortuitously observed nearly along the plane of an opaque circumbinary ring that is, itself, somewhat tilted with respect to the binary’s orbital plane. To orient the reader, a schematic of the KH 15D system is shown in Figure 1. The ring is presumably the inner part ( $< 5$  AU) of a more extensive circumbinary disk (CBD) that provides gas for continuing accretion. The outer disk has recently been detected at mm wavelengths with the SMA (Herbst & Wilner, in preparation). Precession of the ring has, over the past 50 years, gradually occulted the orbit of the binary as projected on the sky. Various studies have shown (e.g., Herbst et al. 2002; Herbst et al. 2010) that the edge of this occulting ring is surprisingly sharp (much less than one stellar radius) and behaves like a knife edge. For a more general discussion of the current properties of the KH 15D light curve and its interpretation, the reader is referred to Herbst et al. (2010).

When first noticed in 1995 (Kearns & Herbst 1998) the occulting edge had just about completely covered the orbit of the more massive star (designated star B following the

nomenclature of W06). From 1995 to 2009 the knife edge moved progressively across the orbit of star A, producing the observed light curve (Hamilton et al. 2005; Herbst et al. 2010). During this time the system exhibited dramatic photometric variations on the orbital cycle as star A regularly rose and set with respect to the ring horizon. Throughout part of this phase of its evolution (2001-2006) we were able to obtain a substantial number of spectra ( $N=48$ ) of the system at a variety of orbital phases and heights of star A above and below the ring edge. This has allowed us to do a kind of “occultation mapping” of gas flows in the magnetosphere of star A and perhaps elsewhere within the inner cavity of the CBD. By far the most useful spectral feature available to us for this work is  $H\alpha$ .

Hamilton et al. (2003) used 3 spectra obtained during one cycle in 2001 to infer the presence of a jet and a magnetospheric accretion flow. At that time, the system was believed to be only a single star with a circumstellar disk containing a warp. In this paper, we present the analysis of additional high resolution spectroscopic data of the KH 15D system, specifically, the  $H\alpha$  emission line profiles, obtained while in its bright state, during ingress/egress, and during eclipse over the course of a 5 year observing period (2001-2006). Section 2 discusses the observations and reductions. The  $H\alpha$  emission line profiles are presented and characterized in Section 3. Profile decompositions based on gaussian fitting and the velocity behavior of the absorption component are discussed in Section 4. The high velocity emission component of the  $H\alpha$  line profile is presented in Section 5, and constraints on the size of the magnetosphere of star A are given in Section 6. General conclusions are drawn in Section 7.

## 2. Observations and Data Reduction

The high resolution echelle spectra analyzed here were obtained during five observing seasons from 2001/2002 through 2005/2006 at various observing facilities. Table 1 gives the UT dates of the observations, telescope/instrument used, wavelength coverage and resolution. We attempted to exploit the “natural coronagraph” that this system represents by focusing primarily on phases during or near ingress and egress, however, spectra were also obtained near mid-eclipse, and when star A was well out of eclipse. Figure 2 shows the Cousins  $I$ -band ( $I_C$ ) data from Hamilton et al. (2005) or Herbst et al. (2010) phased with the orbital period for each of the five observing seasons overlain with the dates on which spectra were obtained. It is clear that the width of the eclipse increased significantly between the beginning and end of the data acquisition period so a particular orbital phase that represented an “out-of-eclipse” observation in 2001/2002 might be “in eclipse” in 2005/2006. This is demonstrated in Figure 3. Each spectrum is characterized, therefore, by two numbers: orbital phase, ranging from  $-0.5$  to  $+0.5$  with  $0.0$  representing the time of mid-eclipse, and the position of

star A with respect to the ring edge, ranging from  $\Delta X = -4$  (4 stellar radii above the edge) to  $\Delta X = +10$  (10 stellar radii below the ring edge). The parameter  $\Delta X$  used here comes from Model 3 of W06<sup>1</sup> and is the elevation of the center of star A above (–) or below (+) the edge of the occulting disk in units of the radius of star A ( $R_A = 1.3 R_\odot = 9 \times 10^8$  m).

As is evident from Table 1, there were five different instruments employed to obtain the observational material analyzed here. These are: the Keck 10-m telescope and High Resolution Echelle Spectrometer (HIRES; solid red lines in Fig. 2), the European Southern Observatory’s 8.2-m Very Large Telescope and UV-Visual Echelle Spectrograph (UVES; long-dashed blue lines), the 2.1-m Otto Struve Telescope at McDonald Observatory and Sandiford Cassegrain Echelle Spectrometer (CE; dash-dot green lines), the 8-m Hobby-Eberly Telescope at McDonald Observatory and High Resolution Spectrograph (HRS; dashed pink lines) and the 6.5-m Magellan II (Clay) Telescope and Magellan Inamori Kyocera Echelle Spectrograph (MIKE; dash-dot-dot-dot orange lines). Brief descriptions of the data and reduction process are now given for each instrument.

## 2.1. The VLT/UVES Spectra

The data obtained with the VLT and UVES used in this analysis were taken during the 2001/2002 and 2004/2005 observing seasons. The data from 2001/2002 were obtained in queue mode and have already been published. The reader is referred to Hamilton et al. (2003) for more information regarding their reduction. The data taken during the 2004/2005 observing season were reduced with a set of custom echelle reduction routines written in IDL. The data reduction procedure is described by Valenti (1994) and Hinkle et al. (2000) and includes bias subtraction, flat fielding by a normalized flat spectrum, scattered light subtraction, and optimal extraction of the spectrum. Due to nebular H $\alpha$  emission near KH 15D, it is important for this study to perform a sky subtraction when reducing the spectra. The VLT/UVES spectral format contains enough room between the orders that background sky spectra are recorded both above and below the stellar spectrum in the slit. The spectral traces defining the order locations for the orders in the stellar spectrum were offset in each direction along the slit and sky spectra were extracted. The two sky spectra were averaged and used to subtract the sky background from the spectra of KH 15D. The wavelength solution was determined by fitting a two-dimensional polynomial

---

<sup>1</sup>Model 3 employs the astrophysical constraint that star A be less massive than star B because it is less luminous. This constraint produces a model that is in best agreement with the observed photometry through 2006.

to  $n\lambda$  as function of pixel and order number,  $n$ , for several hundred extracted thorium lines observed from an internal lamp assembly.

## 2.2. The Keck/HIRES Spectra

Some of the data that were obtained with the Keck I telescope and HIRES for this project were also used as a part of the radial velocity study Johnson et al. (2004). A full description of the reduction procedure used for the Keck data obtained in 2003/2004 is given in that paper. Additional Keck data obtained in Feb 2005 were reduced using the same custom IDL echelle reduction routines referenced above in §2.1. Similar to the VLT/UVES data, sky subtraction was also performed for the Keck/HIRES data.

## 2.3. The McDonald Observatory 2.1-m/CE Spectra

The January 2004 data obtained with the McDonald Observatory 2.1-m Otto Struve Telescope and CE spectrometer were also used as a part of the radial velocity survey presented by Johnson et al. (2004). The reader is again directed to that paper for a full description of the reduction procedures for these spectra.

### 2.3.1. 2.1-m Sky Subtraction

The spectral format of the CE is quite compact, requiring a relatively short slit (in this case 2."5) in order to keep the orders well separated on the CCD. As a result, traditional sky subtraction with this system is not possible. As mentioned above, there is an H $\alpha$  component in the line profiles of KH 15D due to the nebular emission from NGC 2264, the cluster in which KH 15D is located. In order to study the intrinsic variations of the H $\alpha$  profile of KH 15D, it is helpful to remove this nebular component. To do so, we utilized a sky spectrum obtained with one of the HET/HRS spectra of KH 15D (see below) as a proxy for sky subtracting the McDonald 2.1-m CE data. After continuum normalizing the H $\alpha$  order in the 2.1-m CE spectra, we scaled the HET sky spectrum so that when it is subtracted from the 2.1-m CE spectra the nearby [NII]  $\lambda$ 6583 emission line is entirely removed. This line is a pure nebular emission line, so the underlying assumption in this procedure is that the ratio of this line to the nebular H $\alpha$  line stays constant throughout the nebula surrounding KH 15D. As a check on this assumption, we examined the spectra taken with Keck/HIRES which has a long enough slit to separately extract sky spectra on either side of the stellar

spectrum. We scaled the sky spectrum on one side of the stellar spectrum so that the flux in the [NII] line matched that from the sky spectrum taken on the other side of the star. We then differenced the two sky spectra. In each case, no residual H $\alpha$  flux is detected, and the  $3\sigma$  upper limit on the H $\alpha$  flux in the difference spectrum is  $\sim 2\%$  of the nebular H $\alpha$  emission. It thus appears that this is a fairly robust way to remove the sky+nebular emission from the 2.1-m CE spectra.

#### 2.4. The Magellan/MIKE Spectra

The MIKE spectra were reduced with the “MIKE redux” code written by S. Burles, X. Prochaska, and R. Bernstein (see <http://web.mit.edu/~burles/www/MIKE/>). This reduction package performs bias subtraction, flat fielding, order-edge tracing, sky subtraction, and optimal extraction. Wavelength calibration is also performed as part of the package using spectra of a Thorium-Argon arc lamp obtained just prior to each observation of KH 15D. The wavelength solution for the MIKE data was performed with the custom IDL software described above and referenced in Valenti (1994) and Hinkle et al. (2000).

#### 2.5. The HET/HRS Spectra

The HET/HRS spectra used here were all reduced with the custom IDL software described above in §2.1 and referenced in Valenti (1994) and Hinkle et al. (2000). The HRS instrument at the HET is a fiber fed spectrometer. For each observation of KH 15D, sky fibers were placed on either side of the star fiber. As a result of the spectra from these sky fibers appearing on the CCD, the optimal extraction routines in the reduction package were not used. Instead, the counts normal to the dispersion direction were summed at each wavelength in order to produce the extracted spectrum. The observations used here come from two programs looking at KH 15D. As a result, about half the observations used 2'' fibers while the other half used 3'' fibers. The throughput of the fibers used to feed the stellar and sky spectra vary somewhat. As a result, the two sky spectra were summed to increase the signal to noise and the result was then scaled to match the [NII]  $\lambda 6583$  flux in the stellar spectrum before the sky subtraction was performed. Spectra of a Thorium-Argon lamp were also extracted for each night and again a wavelength solution was created by fitting a two-dimensional polynomial to  $n\lambda$  as function of pixel and order number,  $n$ , for several hundred thorium lines.

### 3. The H $\alpha$ Emission Line Profiles

In order to interpret the wealth of complex information produced by the occultation mapping of the H $\alpha$  line profile we required the height of star A above or below the occulting screen, which is taken from Model 3 of W06. Table 2 lists the Julian Date of observation, telescope/instrument, orbital phase, the height of Star A above the disk, the radial velocity (RV) of star A as predicted by W06, the radial velocity of star B as predicted by W06, the calculated or measured (when available) Cousins  $R$  magnitude ( $R_C$ ), the measured  $I_C$  (from Hamilton et al. 2005 or Herbst et al. 2010), the flux ratio used to scale the normalized spectrum, and the barycentric correction.

All profiles have been continuum-fit and normalized to 1.0. Their flux was then scaled in reference to the 2002 December 10 out-of-eclipse spectrum obtained with the HET at McDonald Observatory. The 2002 December 10 spectrum was chosen as the reference spectrum to which all others would be scaled because star A had the largest height above the occulting screen as predicted by the W06 model on that date and presumably represents the H $\alpha$  profile most intrinsic to star A. The scale factor was calculated by computing the difference between the  $R_C$  magnitude on the particular date of interest and the  $R_C$  magnitude observed on 2002 December 10. The flux on 2002 December 10 was assumed to be 1.00. The Cousins  $R$  filter encompasses the wavelength region corresponding to H $\alpha$ , making it the best available proxy for measurement of the flux in the continuum near H $\alpha$ . Actual observed  $R_C$  magnitudes were used when available, however, the majority of the photometric monitoring during these seasons was only done in the Cousins  $I$ -band. When  $R_C$  magnitudes were not available in the photometric database, they were estimated from measured  $I_C$  values using a color-magnitude relation from Hamilton et al. (2005) based on USNO 2002/2003 data. Typical photometric errors are  $\sim 0.01$  out of eclipse and  $\sim 0.1$  in eclipse (Hamilton et al. 2005).

The scaled profiles are shown in Figures 4 and 5. The profiles are plotted from left to right in these figures according to distance above or below the projection of the edge of the occulting disk as calculated by W06. They are shown, in reference to Figure 2, from out of eclipse, through ingress, during mid-eclipse, through egress, and out of eclipse again. The profiles are plotted this way to assist in identifying whether or not there are systematic differences in the profiles given the specific location in the orbit, not just the height above or below the occulting disk. All profiles have been corrected for the Earth’s motion, and are shown in the rest frame of the center of mass of the system.



### 3.1. Characterizing the Variability

When trying to understand the complex variations in the  $H\alpha$  line profiles presented here, one should consider three more or less independent factors influencing the variability: (1) the “edge effect” - occultation by the CBD as measured by the distance  $\Delta X$  with respect to the occulting edge; (2) the “orbital phase effect” - potential variability due to increased accretion on both stars or other changes during certain phases of the eccentric binary orbit (see de Val-Borro et al. 2011 and references therein); and (3) an irregular/chaotic component that is best seen when comparing the profiles taken at similar heights and orbital phase but at different times. We have several multi-day spectral sequences (some with coverage on consecutive days) obtained during ingress, egress, and while the observable star is out of eclipse. These observations occurred over the course of five different observing seasons so we can assess both the short-term and long-term variability of the  $H\alpha$  emission line profile. In the following section, we will begin by demonstrating the changes that are seen in the  $H\alpha$  emission line profile as the stars move throughout their orbits, followed by changes that are produced as star A is occulted by the CBD. Finally, we will discuss variations observed which can be attributed to the irregular nature of the T Tauri accretion process.

#### 3.1.1. Orbital Phase Variations and Occultation Variations

By looking at Figures 4 and 5, it is evident that the KH 15D system exhibits highly variable  $H\alpha$  profiles. We begin our analysis by taking the appropriately scaled (see §3) profiles from Figures 4 and 5 and averaging them according to the predicted distances of star A with respect to the edge of the occulting disk at the time of observation. The spectra were split up into two sets of 7 different bins ( $\Delta X = -4$  to  $-2$ ,  $\Delta X = -2$  to  $-1$ ,  $\Delta X = -1$  to  $0$ ,  $\Delta X = 0$  to  $+1$ ,  $\Delta X = +1$  to  $+2$ ,  $\Delta X = +2$  to  $+4$ , and  $\Delta X = +7$  to  $+10$ ; see Table 3 for details), with the first set of bins for the spectra taken during ingress (approaching mid-eclipse, phases  $-0.5$  to  $0$  according to Figure 2), and the second set of bins for those taken during egress (following mid-eclipse, phases  $0$  to  $+0.5$  according to Figure 2). These sets of averaged profiles are displayed in Figure 6. To orient the reader, “time” in Figure 6 runs down the left hand side of panels and then up the right hand side of panels back to the top.

As one examines the averaged, scaled emission line profiles presented in Figure 6, three distinct “features” can be discerned and are indicated by arrows in the appropriate panels. They are:

1. The absorption component seen mostly out of eclipse and during ingress/egress.

2. The broad component mainly seen once star A is fully occulted.
3. The double peak emission profile primarily observable during full eclipse.

The top four panels in Figure 6 (a-d) represent the out-of-eclipse spectra obtained when  $\Delta X$  ranges from  $-4$  to  $-1$ . The next four panels (e-h) show the ingress and egress spectra obtained when  $\Delta X$  ranges from  $-1$  to  $+1$ . In these eight panels, a “central” absorption feature near velocity = 0 is predominant, and sometimes extends well below the stellar continuum.

The bottom six panels in Figure 6 (i-n) show the averaged  $H\alpha$  profile after the star is completely obscured and at a distance of  $\Delta X = +1$  or greater. Here, we see a generally double-peaked emission line profile, with an underlying broad component. The underlying broad component ranges in velocity from approximately  $-300$  to  $+300$   $\text{km s}^{-1}$ . To emphasize the presence of this faint broad component, which is difficult to see in the regularly scaled plots, the profiles plotted in the bottom 6 panels of Figure 6 have been multiplied by a factor of 10 and over-plotted on the same graph. These modified profiles are shown as a dash-dot-dot-dot line in red. Note that the bottom two panels in Figure 6 (m and n) are identical.

The largest variation in the profiles examined here naturally occurs during the eclipse itself as the star and its magnetosphere sink below, and alternatively rise from behind, the occulting screen. To focus on these phases, we show in Figures 7 and 8, two ingress sequences; one from 2003 February and one from 2004 December. The ingresses are plotted two ways: 1) The top panel shows the fluxed profile with an offset, so that each individual profile is visible. The zero point for each spectrum is indicated by the small horizontal line along the y-axis. 2) The bottom panel shows each spectrum properly fluxed with its continuum adjusted back up to 1.0 so that they can be plotted on top of one another allowing one to see the systematic decline of the flux in the far wings.

Figures 7 and 8 demonstrate that a “typical” ingress spectrum may be characterized as an inverse P Cygni type profile, consisting of red-shifted  $H\alpha$  absorption, superimposed upon blue-shifted  $H\alpha$  emission. We note that the absorption feature starts out extending well below the stellar continuum. As star A sinks below the occulting edge during ingress, the overall photospheric spectrum and all of the absorption that is seen in the  $H\alpha$  profile drops to near zero flux levels.

The profile that is left once the star is fully occulted and several stellar radii below the occulting edge primarily consists of a rather narrow double-peaked emission feature with peaks at  $\sim \pm 30$   $\text{km s}^{-1}$ , as well as an underlying faint broad component ranging in velocity from approximately  $-300$  to  $300$   $\text{km s}^{-1}$ , as mentioned earlier. This double-peaked emission

feature was first noted by Hamilton et al. (2003), and its interpretation in terms of a bipolar jet has been discussed in great detail by Mundt et al. (2010), and will not be further discussed here.

After mid-eclipse, or periastron, star A emerges again, rising from behind the occulting screen during egress. During this phase, we see a more generally enhanced, roughly symmetric, double-peaked  $H\alpha$  emission profile with a slightly blue-shifted absorption feature, as shown in Figure 9. Additionally, Figure 9 shows that during this particular egress, there is a reduction of peak emission flux as more of the star is exposed (i.e., 2005 February 28 vs. 2005 March 01). This seems to be contrary to what one would expect; as more of the star is exposed, more of the  $H\alpha$  emitting region, i.e., the magnetosphere, should be exposed, and therefore a greater amount of  $H\alpha$  flux would be expected. We return to this issue later.

In summary, the disappearance/reappearance of both the “central” absorption feature as well as the overall photospheric spectrum observed in the KH 15D system can be attributed to the effect that the edge of the CBD and its occultation of star A and its close stellar environment has on the observed  $H\alpha$  emission line spectrum. Additionally, the variation from inverse P Cygni profile to double-peaked profile must be dependent on where star A is in its orbit, since the inverse P Cygni profile is mostly observed out of eclipse and into ingress. The significance of these observations will be discussed in §5.

### 3.1.2. *Additional Variability*

T Tauri stars (TTs) are generally characterized by their irregular variability due to accretion and other effects. As a way of assessing the baseline variability of the visible TTS in this system, high-resolution spectra were obtained during the out-of-eclipse phases with the HET during the 2002/2003 (Hessman, PI) and 2005/2006 (Herbst, PI) observing seasons. These data have been scaled by the appropriate flux ratio, had their continua adjusted back up to 1 for ease of comparison, and are shown in Figure 10. The left-hand side of Figure 10 shows the  $H\alpha$  emission line profiles obtained out-of-eclipse in 2002 December and 2003 January/February. The bottom panel shows the 2002/2003 light curve and the vertical lines indicate when the spectra were obtained. The phases are listed in each plot as are the model predicted heights above the edge of the CBD on that given date. On the right-hand side of Figure 10, we show the out-of-eclipse  $H\alpha$  emission line profiles obtained during 2005 December and 2006 February. The bottom panel shows where the spectra were obtained in reference to the 2005/2006 light curve.

Focusing our attention first on the 2002/2003 season, we note that in this season, the

spectra were obtained when star A was located anywhere between  $\sim 3$  and 4 stellar radii above the edge of the CBD (see Figure 3 and Table 3). The phases also range from  $+0.42$  to  $-0.37$ , passing through phase  $\pm 0.5$ . We remind the reader that positive phases are those following mid-eclipse, representing the egress side of the orbit, while negative phases are those preceding mid-eclipse, representing the ingress side of the orbit. A phase of  $\pm 0.5$  is exactly opposite mid-eclipse, which is denoted as phase = 0.

A comparison of the blue-shifted peaks observed in 2002 December and 2003 Jan/Feb does not show a great deal of variation in the maximum flux within the line. In both cases, the relative line flux is  $\sim 2.1$ - $2.2$  at the peak. The maximum flux occurs when the star is at its greatest height ( $\Delta X = -4.02$ , phase =  $-0.48$  for 2002 December, and  $\Delta X = -3.95$ , phase =  $+0.49$  for 2003 January). What is highly variable, however, is the emission, and alternatively, the absorption, in the red-shifted portion of the  $H\alpha$  line profile. The interpretation of this absorption feature and the cause of its variability is discussed in §4.

When comparing the observed profiles obtained during 2005/2006 season, one can see that the maximum flux in the blue-shifted peak in 2005 December is greater than that observed in 2006 February, one full orbital cycle apart, suggesting that this may be the result of the intrinsic variability of TTSs. However, it is important to note that the 2005 December spectra were taken as star A was rising up from the edge of the CBD, as denoted by its X position (phases ranging from 0.38 to 0.46). We see in this set of profiles that as the star continues to rise from behind the edge, the red-shifted emission increases in flux as the blue-shifted emission becomes somewhat narrower and lower in flux. During this time, we also see an increase in the depth of the “central” absorption feature, eventually extending below the continuum.

Comparatively, the profiles obtained in 2006 February (phases ranging from 0.39 to 0.5 and then to  $-0.47$ ) are similar in peak blue-emission flux to the profiles shown on the left-hand side of Figure 10 from 2002/2003. The maximum flux occurs around phase 0.5 when the star is at its greatest predicted height above the occulting edge (2006 February 12). Here we see both blue and red emission with a narrow “central” absorption that extends below the stellar continuum for the first three profiles (2006 February 9, 10, and 12). As the star begins its “descent” back toward the obscuring edge (phases have gone from  $+$  to  $-$ ), the red-shifted emission feature disappears and is replaced by a broad absorption feature, apparently separate from the “central” absorption, and centered around  $+100 \text{ km s}^{-1}$ . This type of change in profile shape is also seen in the top left panel of Figure 10 (2002 December). As star A moves through phase 0.5 and begins its descent to ingress, the profile loses its red-ward emission as it is replaced by a broad red-shifted absorption feature. Note also that the peak blue-emission flux in 2006 February is similar in nature to the peak blue-emission

flux seen in the out-of-eclipse spectra observed in 2002/2003, and shown on the left-hand side of Figure 10.

In summary, the observations show that the  $H\alpha$  emission line profile in the KH 15D system varies systematically with the position of star A in its orbit and as a result of obscuration of the  $H\alpha$  emitting region by the CBD. We see a characteristic inverse P Cygni profile during ingress and a double-peaked, enhanced emission profile during egress. Our observations also reveal that the “central” absorption feature is primarily red-shifted with respect to the systemic velocity during ingress and blue-shifted during egress. Additionally, it appears as if the profile makes its transition from double-peak to inverse P Cygni just as star A passes through phase  $= \pm 0.5$ , or apastron. In the next section, we explore the various components that make up the  $H\alpha$  emission line profile.

#### 4. The Absorption Component

It is clear from Figs. 4 and 5 that there is a substantial, but highly variable absorption component to the  $H\alpha$  profiles when star A is above the occulting edge. Figure 6 shows that this feature depends on the orbital phase of star A. During ingress the central absorption is broad and red-shifted relative to the systemic velocity (see panels a, c, e, and g of Figure 6). During egress, the absorption feature tends to be narrower and more central or slightly blue-shifted (Figure 6, panels b, d, f, and h). Whenever star A is visible above the CBD, the absorption feature extends below the continuum, indicating that the gas responsible for it is at least partly projected onto the stellar photosphere.

To quantify the velocity behavior of the absorption component we have fit the profiles when the star is not fully eclipsed with three gaussians. Normally these were chosen to fit the red and blue emission wings and the central absorption. In one or two cases the red-shifted absorption was so strong that there was no blue emission wing visible and we fit two absorption components. Note that the intention here is to simply help quantify the mean velocity of the absorbing material clearly visible in the profiles. Examples of this fitting are shown in Figure 11, with the combined fit shown as the solid curve in red. Note that in this figure, the left hand panels represents the ingress portion of the orbit, while the right hand panels represents the egress portion of the orbit. Additionally, we draw attention to the fact that the top panels show out of eclipse spectra ( $\Delta X$  values  $\sim +4$ ), while the bottom panels represent spectra when the star was mostly eclipsed ( $\Delta X \sim +0.5$ ). Plotting the profiles in this way helps to identify the differences between ingress and egress.

There is a substantial amount of red-shifted absorption that comes and goes on the

orbital cycle, being strongest during ingress and weaker or perhaps even absent during egress. It is not clear whether there is a separate narrow absorption component centered near the systemic velocity or the velocity of star A. In at least one case shown in Figure 11, where we used two absorption components to model the line, this appears to be the case. The phase-dependent red-shifted component seen during ingress is, however, always present.

Figure 12 shows the velocity of the red-shifted absorption component plotted against binary phase. The top panel shows the velocity of the gas relative to the center of mass of the system, while the bottom panel shows it in the frame of reference of star A. Again, the feature is only visible when at least some portion of star A is above the occulting edge, so there is a gap during perihelion passage. It is quite clear from the figure that as star A becomes visible on the far side of the disk hole from us, the central absorption is redshifted by only a small amount ( $\sim 10 \text{ km s}^{-1}$ ) with respect to star A. But once the star “turns the corner” and starts to move toward the observer on its way to the near side of the gap where it will soon begin to be occulted, the highly red-shifted absorption component appears, with velocities reaching up to  $+100 \text{ km s}^{-1}$  or more.

We believe that this relatively high velocity absorption component is a regular feature of the system that varies with orbital phase, and is not merely a stochastic feature attributable to unsteady accretion. The evidence is that the feature is present in every spectrum during the appropriate orbital phase, even those taken many cycles (and years) apart. It is not always precisely the same strength or velocity, but it is always identifiable as a feature of the  $H\alpha$  profile. This suggests that it is a stable accretion feature (or “stream”) associated with star A.

It is interesting that models of accretion in eccentric binary systems (e.g., de Val-Borro et al. 2011) predict precisely the sort of stable accretion streams that these observations require. In these models, the disk and binary are co-planar, however one can expect the general flow pattern to be rather similar for a slightly inclined system ( $10\text{-}20^\circ$ ). Furthermore, one can expect stronger accretion streams in the inclined system, which may help to understand why this WTTS has such strong accretion signatures. A schematic representation of how such an accretion stream would need to be configured to explain our observations was introduced in Figure 1. Detailed modeling will be required to determine whether such a model satisfies the observations, but an accretion stream does seem promising as a way to understand this absorption component and its variation with orbital phase.

Note that the maximum velocity observed,  $100 \text{ km s}^{-1}$ , is close to the free-fall velocity for gas falling from the inner edge of the CBD near  $0.6 \text{ AU}$  to  $\sim 10$  stellar radii. In this interpretation, then, we would identify the high velocity gas observed during ingress to be material in the accreting stream just outside the magnetosphere. It is quite possible that

the gas accretes onto a disk at this location where it awaits a more rapid transfer to the star (or ejection into a jet) during perihelion passage; see next section). The lower velocity, but still accreting, gas seen during egress and perhaps at all times, may be part of a remnant disk of gas that did not accrete during perihelion passage or the outer parts of the accretion stream. Additionally, since the streams are in co-rotation, when star A is at apastron, gas will be seen approaching with much larger velocities than the star, which would produce a blue-shifted wing. Again, a detailed analysis of these events requires a dynamical model tuned to the properties of the KH 15D system and that is beyond the scope of this work.

## 5. The High Velocity Emission Component

Figure 6 shows clearly that the high velocity wings of the H-alpha profiles vary substantially and systematically with orbital phase. For single CTTSs, this emission is believed to arise within the magnetospheres of stars as they accrete material from a circumstellar disk and its strength is a proxy for the accretion rate. During phases when star A is only partly occulted or entirely visible the high velocity component is associated with its magnetosphere. At other phases there may be a contribution from star B or from the combined magnetospheres. During these fully occulted phases much, if not all, of the light reaches us by reflection from the back wall of the CBD (Herbst et al. 2008), allowing us to observe phenomena occurring during perihelion passage that would otherwise be invisible.

The data show an interesting and clear trend that repeats in all cycles observed. Namely, we observe that the high velocity emission is more intense following perihelion passage (i.e. during egress) than it is prior to perihelion passage (i.e. during ingress). This may be seen by comparing the left hand side of Figure 6, corresponding to ingress, and the right hand side, corresponding to egress. The effects are particularly noticeable in panels near the bottom that apply to the fully occulted system just before and just after perihelion passage. On the left hand panels, one clearly sees the high velocity emission but it is nowhere near as intense as it is on the right hand panels. To make this clearer we have multiplied the relevant profiles by a factor of ten in the bottom six panels.

Another way to demonstrate this point is to compare individual profiles obtained at the same locations with respect to the occulting disk and determine whether the ingress profiles look different from the egress profiles. This direct comparison is shown in Figure 13 where the spectra have been properly fluxed and had their continuum adjusted back up to 1.0, and for two different values of  $\Delta X$  where we happened to have both ingress and egress spectra. It is clear that at both locations relative to the occulting disk (partly visible,  $\Delta X \sim +0.5$ , top panel, and fully occulted,  $\Delta X = +1.09$ , bottom panel) the magnetospheric emission is

more intense during egress than ingress. This will be quantified further in the next section where we discuss the equivalent widths of the blue emission wing in more detail.

We note that in addition to the phase-dependent variations discussed above there is clearly a time-dependent variation as well. It is not the case that every egress spectrum looks identical in its profile to others obtained at the same orbital phase. This time variability is illustrated in Figure 14 where we show some egress spectra obtained near the same orbital phase and at times when star A was fully occulted, or nearly so. These spectra are of somewhat lower resolution than many but serve to make the main point: there is substantial variation in the emission line wings that is independent of orbital phase or location relative to the occulting disk edge. The 2001 Dec 20 spectrum is particularly notable, and was discussed in Hamilton et al. (2003) in the context of magnetospheric accretion. Here we see a very extended and substantial wing indicating that during this perihelion passage there was a substantial amount of activity.

In Figure 15 we show a sequence of spectra taken during a single egress while the system was fully occulted. Here, also, we see substantial variability in the high velocity emission, now on a daily timescale. There is some evidence for a high velocity “feature” that shows up as a small bump in the blue wing on 2005 Dec 12 and migrates to lower velocity and higher intensity by 2005 Dec 12. Whether this is related to the changing aspect of the star caused by stellar rotation and orbital motion or to some feature of the accretion is unknown. It is clear, however, that there is variability in the magnetospheric emission even on timescales as short as a day.

Our observations appear to confirm a general prediction of models of the binary accretion process in eccentric systems (Artymowicz & Lubow 1996; Günther & Kley 2002; and de Val-Borro et al. 2011) that accretion onto the stars occurs predominantly during periastron. It is during egress, i.e. after perihelion passage, that we see the most activity in the high velocity wings of the line and the greatest intensity overall. Similar results have been reported for DQ Tau (whose binary parameters are very similar to those for KH 15D; see Table 4) by Mathieu et al. (1997) and Basri et al. (1997), for V4046 Sgr by Stempels & Gahm (2004), for UZ Tau E by Jensen et al. (2007), and for V773 Tau A by Boden et al. (2007).

In some cases mentioned above, the evidence for pulsed accretion includes phase-dependent continuum variations detected by broad band photometric studies. It has long been known that KH 15D shows a brightening near perihelion passage (see Hamilton et al. 2001; Hamilton et al. 2005; Herbst et al. 2010) at  $I_C$  and some variations in color. The general phenomenon has been interpreted as the influence of star B, which is inferred to be the brighter of the pair, reaching its greatest extension toward the edge of the CBD at perihelion. At these orbital phases it, therefore, becomes the dominant source of the reflected light. It could, of



course, be that some of this variation is caused by an increased brightness of one or both stars during perihelion passage. If the accretion is primarily onto the lower mass star (star A), we may not be able to witness the more dramatic brightness enhancements that occur, because star A is at its lowest point with respect to the disk edge then and perhaps completely invisible to us, even by reflected light. This would, however, be in contrast to the current models, which predict that mass is preferentially channeled to the primary. Although the photometry cannot directly confirm the case for increased accretion during perihelion passage in the case of KH 15D, they are certainly not inconsistent with the spectroscopic evidence reported here.

## 6. Constraints on the Size of the Magnetosphere of Star A

Our data taken during eclipses can, at most, be used to constrain the size of the magnetosphere of star A in the vertical direction. As outlined in previous papers (e.g., Herbst et al. 2002) the occulting edge of the circumbinary disk/ring is extremely “sharp,” i.e., the transition region from optically thin to optically thick is less than  $\sim 0.1 R_A$  (and perhaps much less) so that the eclipses can be modeled with a “knife-edge.” The magnetospheric emission model profiles of Hartmann and collaborators (Hartmann et al. 1994; Muzerolle et al. 1998; Muzerolle et al. 2001) show that the blue wing of these profiles is an emission component, while the red wing has contributions from both emission and absorption. We have calculated the emission flux and equivalent width of the blue-shifted wing of the  $H\alpha$  profile between  $-280 \text{ km s}^{-1}$  and  $-85 \text{ km s}^{-1}$ , ignoring the velocity range from 0 to  $-85 \text{ km s}^{-1}$  because it is likely affected by emission from the jet. For velocities less than  $-280 \text{ km s}^{-1}$ , there is very little emission.

In Figure 16 we show the fluxes (top panel) and equivalent width (lower panel) for two eclipse sequences obtained during ingress (2003 Feb and 2004 Dec; red squares and blue triangles, respectively) and two eclipse sequences obtained during egress (2005 Feb and 2005 Dec; green stars and pink circles, respectively). Each ingress or egress is indicated in the upper left corner of the figure, and the change in position from the center of mass of the binary of star A ( $r$ ) is indicated for each ingress/egress shown. For reference, the binary semi-major axis is  $0.25 \text{ AU} = 41.4 R_A$ . Note that for the ingress observations, time increases from left to right, while for the egress observations it is just the opposite. To interpret the data displayed in Figure 16, we make use of the “knife-edge” model, and assume that the emission region is spherically symmetric and homogeneously emitting as an initial thought experiment.

We begin with the top panel of Figure 16, which shows the blue wing emission flux.

Within the knife-edge model, the somewhat rapid decrease of the relative line fluxes during ingress can be most easily explained by a decreasing geometrical size of the emission region (i.e., less of the emission region is exposed as star A “sets” below the edge of the occulting disk), provided this region is not highly variable on time scales of a few days. In principal, most of the flux data for the two egress phases can be explained in the same way. However, for the 2005 December egress, there is also a strong time variable component superimposed, which causes a strong decline in the line flux for the end of the egress phase (recall that for egress, increasing time runs from right to left). As already outlined elsewhere in this paper (see §5) the line fluxes during egress are typically a factor 3 higher than during ingress, which has been attributed to increased accretion from the circumbinary disk/ring onto the two stars at the time near or after periastron passage.

To constrain the size of the  $H\alpha$  emission region *relative to the size of the stellar disk*, we use the equivalent width (EW) of the emission contained within the velocity range of  $-85$  to  $-280 \text{ km s}^{-1}$ , because the EW is a measure of the *ratio* between line flux and continuum flux. To interpret the EW measurements within the context of the above mentioned “knife-edge” model, assuming a spherically symmetric emission line region, we consider two extreme cases: 1) the case of an emission region that is at least a few times larger than the stellar disk, and 2) the other extreme where the emission region is not extended and is roughly the same size as the stellar disk.

In the first case, the EW should increase between  $\Delta X = 0$  and  $\Delta X = +1$ , because at  $\Delta X = +1$ , all of the stellar disk is effectively covered and the only continuum emission visible would be that due to the scattered component. If the emission region were indeed larger than the stellar disk, say with a radius of  $2R_A$ , only a fraction of that region would be covered. Therefore, the ratio between emission line flux and continuum flux should be highly increased. We do, in fact, see a slight increase in the EW between  $\Delta X = 0$  and  $\Delta X = +1$  for both ingresses, however, it is more pronounced for the 2003 Feb ingress. If instead, we examine the second case where the emitting region is roughly the same size as the stellar disk, we would not expect a change in the EW at all. It is difficult to interpret the observed EW measurements in exactly this way, though the relatively small change in EW suggests a relatively small magnetosphere.

The egress data displayed in Figure 16 show that during egress the EW of  $H\alpha$  is about a factor of 2-4 greater than during ingress. This means that within the simplified spherically symmetric model considered here either the radius or the surface brightness of the line emission region has increased. Unfortunately, the egress data are not well sampled between  $\Delta X = 0$  and  $\Delta X = +1$  in order to check whether the radius of the emission line region has indeed increased. The 2005 Feb egress data suggest that there is a factor of 2 decrease in

EW from  $\Delta X = +1$  to  $+0.5$ , but this rests on only one data point. In 2005 Dec, the same sort of trend is seen (decreasing EW as the star moves closer to the occulting edge) but the trend is not as steep for that egress, and the EW is on average greater.

The EW data in Figure 16 can only constrain the extended emission perpendicular to the knife edge since it is believed that star A moves roughly up and down with respect to the occulting edge. We cannot exclude a disk-like emission region around the star with a disk of e.g. several stellar radii in size. In fact, in the models of Hartmann et al. (1994), the vertical extent of their magnetospheric accretion flow is barely bigger than the star, however, the magnetosphere extends out to  $2\text{--}3 R_\star$ . At most, we can argue that this disk like structure could be roughly 10-15% thicker than the stellar diameter (in the direction perpendicular to the knife edge).

If the  $H\alpha$  emitting region were uniformly bright, we would expect that the EW measurements for both ingress and egress to be the same. We show in Figure 17, the flux (top panel) and EW (bottom panel) of the  $H\alpha$  emission contained within the velocity range of  $-85$  to  $-280 \text{ km s}^{-1}$  for all observed profiles. Open symbols represent ingress measurements, while filled symbols represent egress measurements. Here we see a generally increasing EW for ingress from  $\Delta X = 0$  to  $\Delta X = +1$ , and that all egress measurements are a factor of 2-4 times greater than ingress measurements.

If we take the EW of the  $H\alpha$  emitting region as a proxy for accretion rate, we can conclude that the accretion rate onto star A has increased significantly after periastron (phase = 0). This has been modeled for eccentric binaries and is shown in Figure 2 of Artymowicz & Lubow (1996), Figure 12 of Günther & Kley (2002), and de Val-Borro et al. (2011). Both Günther & Kley (2002) and de Val-Borro et al. (2011) model the DQ Tau system, which can be used as a proxy for the KH 15D system (see Table 4). All models demonstrate that the accretion rates are greater during periastron passage, however, both Artymowicz & Lubow (1996) and Günther & Kley (2002) show that the peak accretion occurs just prior to periastron passage.

To compare our results to those presented in Figure 2 of Artymowicz & Lubow (1996), we plot our EW measurements as a function of phase and approximated their model for gas accretion rate as a simple gaussian. Figure 18 shows that if we scale the gaussian to match our data on ingress (solid red line), we cannot match the egress accretion rate. If instead, we scale the gaussian to match our egress data, we cannot match the ingress observations (dashed blue line). This suggests that the simulation does not quite accurately predict the timing of the increase in accretion, or there may be something significant within the KH 15D system that is not included within the model, like a differential occultation of the magnetosphere. The early calculations by Artymowicz & Lubow (1996) used here were based

on smooth particle hydrodynamics and rather coarse. A new theoretical approach to this problem is warranted.

## 7. Conclusions

Our spectroscopic studies have revealed intrinsic variability and amazing structure in the  $H\alpha$  line profiles caused by high velocity gas flows in the vicinity of the stars within the KH 15D system. The profiles observed during ingress and egress are distinctly different, changing from an inverse P-Cygni profile during ingress to an enhanced double-peaked profile with broad extended wings during egress. The differences in these profiles can be understood in terms of models of accretion flows within an eccentric binary (Artymowicz & Lubow 1996; Günther & Kley 2002; and de Val-Borro et al. 2011). Measurements of the flux and EW of the blue-shifted emission located in the wings of  $H\alpha$  (velocity ranging from  $-280 \text{ km s}^{-1}$  to  $-85 \text{ km s}^{-1}$ ) give us an indication that the  $H\alpha$  emitting region is compact and variable in brightness on the time scale of the orbital period.

There is potentially a great deal more information locked in these spectra than we have been able to extract. The present study will hopefully serve as an incentive and guide to more detailed modeling. The dynamics of the binary system are very well understood (W06) and it should be quite possible to model with definiteness the expected gas flows and accretion dynamics using codes that have already been applied to similar systems. These data could potentially serve as a critical test of such models. Some subtleties of the profile variations have undoubtedly escaped us and comparison with models of this particular system may reveal them.

We would like to thank the anonymous referee for the suggested improvements to this paper. We also thank Dr. Frederic V. Hessman for graciously allowing us to use the data he collected with the HET. C.M.H would like to thank Dr. Eric Mamajek and Dr. David James for helpful advice and discussions regarding the creation of Figure 1. C.M.H. acknowledges partial support by the American Association of University Women through an American Fellowship. C.M.J.-K. acknowledges partial support by the NASA Origins of Solar Systems program through the following grants to Rice University: NNX08AH86G and NNX10AI53G. W.H. acknowledges partial support by the NASA Origins of Solar Systems program. Some of the data presented herein were obtained at the W. M. Keck Observatory, which is operated as a scientific partnership among the California Institute of Technology, the University of California, and the National Aeronautics and Space Administration. The Observatory was made possible by the generous financial support of the W.M. Keck Foun-

dation. The authors wish to recognize and acknowledge the very significant cultural role and reverence that the summit of Mauna Kea has always had within the indigenous Hawaiian community. We are most fortunate to have the opportunity to conduct observations from this mountain. The Hobby-Eberly Telescope (HET) is a joint project of the University of Texas at Austin, the Pennsylvania State University, Stanford University, Ludwig-Maximilians-Universität München, and Georg-August-Universität Göttingen. The HET is named in honor of its principal benefactors, William P. Hobby and Robert E. Eberly. This paper is based in part on observations collected at the European Southern Observatory (Program 074.C- 0604A). C.M.H. would also like to thank Darla and Steve McKee, as well as the Masci family, for graciously supporting her and her daughter throughout the beginning, and final production, of this work, respectively. This paper is dedicated to Robert Masci.

## REFERENCES

- Agol, E., Barth, A. J., Wolf, S., & Charbonneau, D. 2004, *ApJ*, 600, 781
- Artymowicz, P. & Lubow, S. H. 1996, *ApJ*, 467, L77
- Barge, P. & Viton, M. 2003, *ApJ*, 593, L117
- Barsunova, O. Yu., Grinin, V. P., & Sergeev, S. G. 2005, *Ap*, 48, 1
- Basri, G., Johns-Krull, C. M. & Mathieu, R. D. 1997 *AJ*, 114, 781
- Boden, A. F., Torres, G., Sargent, A. I., et al. 2007, *ApJ*, 670, 1214
- Chiang, E. I., & Murray-Clay, R. A. 2004, *ApJ*, 607, 913
- Deming, D., Charbonneau, D., Harrington, J. 2004, *ApJ*, 601, L87
- de Val-Borro, M., Gahm, G. F., Stempels, H. C., & Pepliński, A. 2011, *MNRAS*, 413, 2679
- Günther, R., & Kley, W. 2002, *A&A*, 387, 550
- Hamilton, C. M., Herbst, W., Ferro, A. J., & Shih, C. 2001, *ApJ*, 554, L201
- Hamilton, C. M., Herbst, W., Mundt, R., Bailer-Jones, C. A. L., & Johns-Krull, C. M. 2003, *ApJ*, 591, L45
- Hamilton, C. M., Herbst, W., Vrba, F. J., Ibrahimov, M. A., Mundt, R., Bailer-Jones, C. A. L., Filippenko, A. V., Li, W., Béjar, V. J. S., Ábrahám, P. et al. 2005, *AJ*, 130, 1896

- Hartmann, L., Hewett, R., & Calvet, N. 1994, *ApJ*, 426, 669
- Herbst, W., et al. 2002, *PASP*, 114, 1167
- Herbst, W., Hamilton, C. M., Leduc, K., Winn, J. N., Johns-Krull, C. M., Mundt, R., and Ibrahimov, M. 2008, *Nature*, 452, 194
- Herbst, W., LeDuc, K., Hamilton, C. M., Winn, J. N., Ibrahimov, M., Mundt, R., Johns-Krull, C. M. 2010, *AJ*, 140, 2025
- Hinkle, K., Wallace, L., Valenti, J., & Harmer, D. 2000, *Visible and Near Infrared Atlas of the Arcturus Spectrum 3727-9300 Å* ed. K. Hinkle, L. Wallace, J. Valenti, & D. Harmer. (San Francisco: ASP) ISBN: 1-58381-037-4
- Jensen, E. L. N., Saurav, D., Stassun, K. G., Patience, J., Herbst, W., Walter, F. M., Simon, M., & Basri, G. 2007, *AJ*, 134, 241
- Johnson, J. A., Marcy, G. W., Hamilton, C. M., Herbst, W., & Johns-Krull, C. M. 2004, *AJ*, 128, 1265
- Johnson, J. A., & Winn, J. N. 2004, *AJ*, 127, 2344
- Johnson, J. A., Winn, J. N., Rampazzi, F., Barbieri, C., Mito, H., Tarusawa, K., Tsvetkov, M., Borisova, A., & Meusinger, H. 2005, *AJ*, 129, 1978
- Kearns, K. E., & Herbst, W. 1998, *AJ*, 116, 261
- Kusakabe, N., Tamura, M., Nakajima, Y., Kandori, R., et al. 2005, *ApJ*, 632, L139
- Maffei, P., Ciprini, S., & Tosti, G. 2005, *MNRAS*, 357, 1059
- Mathieu, R. D., Stassun, K., Basri, G., Jensen, E. L. N., Johns-Krull, C. M., Valenti, J. A., & Hartmann, L. W. 1997, *AJ*, 113, 1841
- Mundt, R., Hamilton, C. M., Herbst, W., Johns-Krull, C. M., & Winn, J. N. 2010, *ApJ*, 708, L5
- Muzerolle, J., Calvet, N., & Hartmann, L. 1998, *ApJ*, 492, 743
- Muzerolle, J., Calvet, N., & Hartmann, L. 2001, *ApJ*, 550, 944
- Stempels, H. C., & Gahm, G. F. 2004, *Å*, 421, 1159
- Tokunaga, A. T., et al. 2004, *ApJ*, 601, L91

- Valenti, J. A. 1994, Ph.D.Thesis, University of California, Berkeley
- Winn, J. N., Garnavich, P. M., Stanek, K. Z., & Sasselov, D. D. 2003, ApJ, 593, L121
- Winn, J. N., Holman, M. J., Johnson, J. A., Stanek, K. Z., & Garnavich, P. 2004, ApJ, 603, L45
- Winn, J. N., Hamilton, C. M., Herbst, W., Hoffman, J. L., Holman, M. J., Johnson, J. A., & Kuchner, M. J. 2006, ApJ, 644, 510

Table 1. Spectroscopic Observations of KH 15D

UT Date	Telescope/Instrument	Wavelength Coverage (Å)	$\lambda/\Delta\lambda$
2001 Nov 29	VLT/UVES	4800-6800	44,000
2001 Dec 14	VLT/UVES	4800-6800	44,000
2001 Dec 20	VLT/UVES	4800-6800	44,000
2002 Dec 06	HET/HRS	6380-7330 <sup>a</sup>	15,000
2002 Dec 10	HET/HRS	6380-7330 <sup>a</sup>	15,000
2002 Dec 13	HET/HRS	6380-7330 <sup>a</sup>	15,000
2003 Jan 23	HET/HRS	6380-7330 <sup>a</sup>	15,000
2003 Jan 26	HET/HRS	6380-7330 <sup>a</sup>	15,000
2003 Feb 02	HET/HRS	6380-7330 <sup>a</sup>	15,000
2003 Feb 05	HET/HRS	6380-7330 <sup>a</sup>	15,000
2003 Feb 08	Keck/HIRES	4200-6600	70,000
2003 Feb 09	Keck/HIRES	4200-6600	70,000
2003 Feb 10	Keck/HIRES	4200-6600	70,000
2003 Mar 06	HET/HRS	6380-7330 <sup>a</sup>	15,000
2003 Mar 23	HET/HRS	6380-7330 <sup>a</sup>	15,000
2003 Dec 16	Keck/HIRES	4400-6800	40,000
2003 Dec 18	Keck/HIRES	4400-6800	40,000
2004 Jan 04	McD/CE	5600-6900	30,000
2004 Jan 05	McD/CE	5600-6900	30,000
2004 Jan 10	McD/CE	5600-6900	30,000
2004 Feb 05	Keck/HIRES	4400-6800	39,000
2004 Mar 10	Keck/HIRES	4700-7100	40,000
2004 Mar 12	Keck/HIRES	4800-7100	40,000
2004 Dec 10	McD/CE	5600-6900	30,000
2004 Dec 13	VLT/UVES	5800-7300	44,000
2004 Dec 14	VLT/UVES	5900-7300	44,000
2004 Dec 15	VLT/UVES	5800-7300	44,000
2004 Dec 16	VLT/UVES	5800-7300	55,000
2004 Dec 17	VLT/UVES	5800-7300	55,000
2004 Dec 18	VLT/UVES	5800-7300	55,000
2005 Feb 27	Keck/HIRES	4800-7100	42,000
2005 Feb 28	Keck/HIRES	4800-7100	42,000
2005 Mar 01	Keck/HIRES	4800-7100	42,000
2005 Dec 12	Mag/MIKE	5800-6800	25,000
2005 Dec 13	Mag/MIKE	5800-6800	25,000
2005 Dec 14	Mag/MIKE	5800-6800	25,000
2005 Dec 15	Mag/MIKE	5800-6800	25,000
2005 Dec 20	HET/HRS	5880-6770 <sup>b</sup>	30,000
2005 Dec 21	HET/HRS	5880-6770 <sup>b</sup>	30,000
2005 Dec 22	HET/HRS	5880-6770 <sup>b</sup>	30,000
2005 Dec 23	HET/HRS	5880-6770 <sup>b</sup>	30,000
2005 Dec 24	HET/HRS	5880-6770 <sup>b</sup>	30,000
2006 Feb 07	HET/HRS	5880-6770 <sup>b</sup>	30,000
2006 Feb 09	HET/HRS	5880-6770 <sup>b</sup>	30,000
2006 Feb 10	HET/HRS	5880-6770 <sup>b</sup>	30,000
2006 Feb 12	HET/HRS	5880-6770 <sup>b</sup>	30,000
2006 Feb 13	HET/HRS	5880-6770 <sup>b</sup>	30,000
2006 Feb 14	HET/HRS	5880-6770 <sup>b</sup>	30,000

<sup>a</sup>These wavelengths were covered on the blue chip. In addition, the wavelength region 7480-8320 Å was covered on the red chip.

<sup>b</sup>These wavelengths were covered on the blue chip. In addition, the wavelength region 6880-7800 Å was covered on the red chip.



Table 2. Parameters Used to Plot and Scale the H $\alpha$  Emission Line Profiles Shown in Figures 4 and 5.

Julian Date	Telescope/Instrument	Orbital Phase <sup>a</sup>	Position of Star A <sup>b</sup>	$RV_A^b$ km s <sup>-1</sup>	$RV_B^b$ km s <sup>-1</sup>	$R^c$	$I^d$	Flux Ratio <sup>e</sup>	Barycentric Correction km s <sup>-1</sup>
2452242.7446	VLT/UVES	-0.26	-1.46	-9.95	4.52	15.28	14.49	0.990	16.23
2452257.8271	VLT/UVES	0.05	8.74	59.86	-27.21	18.86	18.18	0.036	9.10
2452263.7026	VLT/UVES	0.17	1.95	-2.19	0.99	18.31	17.61	0.060	6.35
2452614.9333	HET/HRS	0.44	-3.90	-18.89	8.58	15.25	14.48	1.020	12.80
2452618.9292	HET/HRS	-0.48	-4.02	-18.43	8.61	15.27	14.50	1.000	10.89
2452621.7431	HET/HRS	-0.43	-3.65	-17.34	7.88	15.26	14.49	1.010	9.90
2452662.6451	HET/HRS	0.42	-3.68	-18.83	8.55	15.25	14.48	1.020	-10.68
2452665.8014	HET/HRS	0.49	-3.95	-18.76	8.52	15.25	14.48	1.020	-12.51
2452672.6090	HET/HRS	-0.37	-2.91	-15.82	7.18	15.29	14.52	0.980	-15.23
2452675.7688	HET/HRS	-0.31	-1.71	-12.99	5.90	15.29	14.52	0.980	-16.92
2452678.8193	Keck/HIRES	-0.26	-0.12	-8.94	4.06	15.57	14.80	0.760	-18.29
2452679.8276	Keck/HIRES	-0.24	0.50	-7.20	3.27	16.20	15.46	0.420	-18.71
2452680.8356	Keck/HIRES	-0.22	1.17	-5.15	2.42	18.09	17.39	0.070	-19.13
2452704.6771	HET/HRS	0.29	-1.39	-15.35	6.97	15.33	14.56	0.950	-26.23
2452721.6361	HET/HRS	-0.36	-2.59	-15.33	6.96	15.28	14.46	0.990	-28.70
2452990.0431	Keck/HIRES	0.18	2.72	-4.83	2.19	18.29*	17.62	0.060	7.84
2452992.0413	Keck/HIRES	0.22	1.09	-10.63	4.83	18.11*	17.42	0.070	6.84
2453008.7960	McD/CE	-0.42	-2.71	-17.33	7.87	15.25	14.47	1.020	-1.33
2453009.8729	McD/CE	-0.40	-2.48	-16.74	7.60	15.22	14.44	1.050	-2.06
2453014.7920	McD/CE	-0.30	-0.77	-12.58	5.71	15.34	14.57	0.940	-4.42
2453040.8025	Keck/HIRES	0.22	0.92	-11.45	5.20	18.24	17.56	0.060	-16.88
2453074.7882	Keck/HIRES	-0.07	7.61	23.23	-10.56	18.85*	18.25	0.040	-27.41
2453076.8125	Keck/HIRES	-0.03	9.36	42.73	-19.43	18.51*	17.81	0.050	-27.79
2453349.8684	McD/CE	-0.38	-1.31	-15.86	7.20	15.28	14.51	0.990	10.85
2453352.7976	VLT/UVES	-0.31	-0.28	-13.29	6.03	15.35	14.59	0.930	9.56
2453353.6774	VLT/UVES	-0.29	0.11	-12.31	5.59	15.51	14.74	0.800	9.28
2453354.7199	VLT/UVES	-0.27	0.60	-11.01	5.00	16.35	15.60	0.370	8.73
2453355.6510	VLT/UVES	-0.25	1.09	-9.69	4.40	17.55	16.85	0.120	8.32
2453356.6724	VLT/UVES	-0.23	1.66	-8.04	3.65	17.89	17.20	0.090	7.80
2453357.6852	VLT/UVES	-0.21	2.28	-6.16	2.79	18.20	17.50	0.067	7.28
2453428.8268	Keck/HIRES	0.26	1.09	-13.25	6.02	17.31	16.60	0.150	-24.91
2453429.8250	Keck/HIRES	0.28	0.52	-14.70	6.67	15.86	15.10	0.580	-25.18
2453430.8201	Keck/HIRES	0.30	0.02	-15.84	7.19	15.47	14.70	0.830	-25.45
2453716.7708	Mag/MIKE	0.21	3.31	-8.20	3.72	18.80	18.13	0.040	9.98
2453717.7708	Mag/MIKE	0.23	2.58	-10.71	4.86	18.27	17.59	0.060	9.49
2453718.7708	Mag/MIKE	0.25	1.93	-12.69	5.76	18.14	17.45	0.070	9.00
2453719.7708	Mag/MIKE	0.27	1.35	-14.25	6.47	17.60	16.90	0.120	8.51
2453724.7264	HET/HRS	0.38	-0.63	-18.26	8.30	15.38	14.61	0.900	6.35
2453725.7340	HET/HRS	0.40	-0.87	-18.59	8.44	15.31	14.52	0.960	5.83
2453726.7222	HET/HRS	0.42	-1.05	-18.79	8.53	15.28	14.51	0.990	5.35
2453727.7181	HET/HRS	0.44	-1.19	-18.89	8.58	15.27	14.50	1.000	4.84
2453728.7090	HET/HRS	0.46	-1.28	-18.90	8.58	15.22	14.45	1.050	4.35
2453773.7556	HET/HRS	0.39	-0.67	-18.49	8.40	15.49	14.73	0.820	-17.81
2453775.7458	HET/HRS	0.43	-1.03	-18.86	8.57	15.34	14.57	0.940	-18.59
2453776.5862	HET/HRS	0.45	-1.12	-18.91	8.59	15.28	14.50	0.990	-18.59
2453778.7409	HET/HRS	0.50	-1.21	-18.72	8.51	15.23	14.46	1.040	-19.74
2453779.5889	HET/HRS	-0.49	-1.19	-18.55	8.43	15.25	14.48	1.020	-19.74
2453780.7305	HET/HRS	-0.47	-1.12	-18.22	8.28	15.26	14.49	1.010	-20.45

- <sup>a</sup>The orbital phase was calculated using the following ephemeris for mideclipse:  $\text{JD (mideclipse)} = 2,453,077.59 + 48.37E$ .
- <sup>b</sup>These values come from Model 3 of Winn et al. (2006). The height above the disk is given in units of the radius of star A. The model predicted systemic velocity of  $18,676 \text{ km s}^{-1}$  has been subtracted out of the radial velocities to put them in the reference frame of the system.
- <sup>c</sup>The  $R$  magnitudes were either measured directly (marked with an asterisk) or calculated using the following relation derived from the 2002/2003 color data from Hamilton et al. (2005):  $R-I = 1.18301 - 0.0283473 \cdot I$ .
- <sup>d</sup>The  $I$  magnitudes were taken from Hamilton et al. (2005) except for the 2005/2006 observing season, which were taken from Herbst et al. (2010).
- <sup>e</sup>The flux ratios were calculated relative to the 2002 December 10 ( $\text{JD} = 2452721.6361$ ) observation because it has the highest calculated position above the disk as predicted by Model 3 of Winn et al. (2006), and therefore, is presumably the least obscured observation.

Table 3. Dates and predicted heights for spectra included in each distance bin presented in Figure 6.

Distance Bin	UT Date	Height ( $R_*$ )	Obs/Instr
$\Delta X = -4$ to $-2$ (ingress)	2002 Dec 10	-4.02	HET/HRS
	2002 Dec 13	-3.65	HET/HRS
	2003 Feb 02	-2.91	HET/HRS
	2004 Jan 04	-2.71	McD/CE
	2003 Mar 23	-2.59	HET/HRS
$\Delta X = -2$ to $-1$ (ingress)	2004 Jan 05	-2.48	McD/CE
	2003 Feb 05	-1.71	HET/HRS
	2001 Nov 29	-1.46	VLT/UVES
	2004 Dec 10	-1.31	McD/CE
	2006 Feb 13	-1.19	HET/HRS
$\Delta X = -1$ to $0$ (ingress)	2006 Feb 14	-1.12	HET/HRS
	2004 Jan 10	-0.77	McD/CE
	2004 Dec 13	-0.28	VLT/UVES
	2003 Feb 08	-0.12	Keck/HIRES
	2004 Dec 14	0.11	VLT/UVES
$\Delta X = 0$ to $1$ (ingress)	2003 Feb 09	0.50	Keck/HIRES
	2004 Dec 15	0.60	VLT/UVES
$\Delta X = 1$ to $2$ (ingress)	2004 Dec 16	1.09	VLT/UVES
	2003 Feb 10	1.17	Keck/HIRES
	2004 Dec 17	1.66	VLT/UVES
$\Delta X = 2$ to $4$ (mid-eclipse)	2004 Dec 18	2.28	VLT/UVES
	2004 Mar 10	7.61	Keck/HIRES
	2001 Dec 14	8.74	VLT/UVES
	2004 Mar 12	9.36	Keck/HIRES
$\Delta X = 4$ to $2$ (egress)	2005 Dec 12	3.31	Magellan/MIKE
	2003 Dec 16	2.72	Keck/HIRES
	2005 Dec 13	2.58	Magellan/MIKE
$\Delta X = 2$ to $1$ (egress)	2001 Dec 20	1.95	VLT/UVES
	2005 Dec 14	1.93	Magellan/MIKE
	2005 Dec 15	1.35	Magellan/MIKE
	2005 Feb 27	1.10	Keck/HIRES
	2003 Dec 18	1.09	Keck/HIRES
$\Delta X = 1$ to $0$ (egress)	2004 Feb 05	0.92	Keck/HIRES
	2005 Feb 28	0.52	Keck/HIRES
	2005 Mar 01	0.02	Keck/HIRES
$\Delta X = 0$ to $-1$ (egress)	2005 Dec 20	-0.63	HET/HRS
	2006 Feb 07	-0.67	HET/HRS
	2005 Dec 21	-0.87	HET/HRS
$\Delta X = -1$ to $-2$ (egress)	2006 Feb 09	-1.03	HET/HRS
	2005 Dec 22	-1.05	HET/HRS
	2006 Feb 10	-1.12	HET/HRS
	2005 Dec 23	-1.19	HET/HRS
	2006 Feb 12	-1.21	HET/HRS
$\Delta X = -2$ to $-4$ (egress)	2005 Dec 24	-1.28	HET/HRS
	2003 Mar 06	-1.39	HET/HRS
	2003 Jan 23	-3.68	HET/HRS
	2002 Dec 06	-3.90	HET/HRS
	2003 Jan 26	-3.95	HET/HRS



Table 4. Orbital Parameters for DQ Tau and KH 15D.

Binary System	Period (days)	$M_2/M_1$	$e$	$a$ (AU)	$i$
DQ Tau <sup>a</sup>	15.804	0.97	0.56	0.13	23°
KH 15D <sup>b</sup>	48.38	0.83	0.57	0.25	92.5°

<sup>a</sup>Parameters for DQ Tau come from Mathieu et al. 1997.

<sup>b</sup>Parameters for KH 15D come from Model 3 of W06.

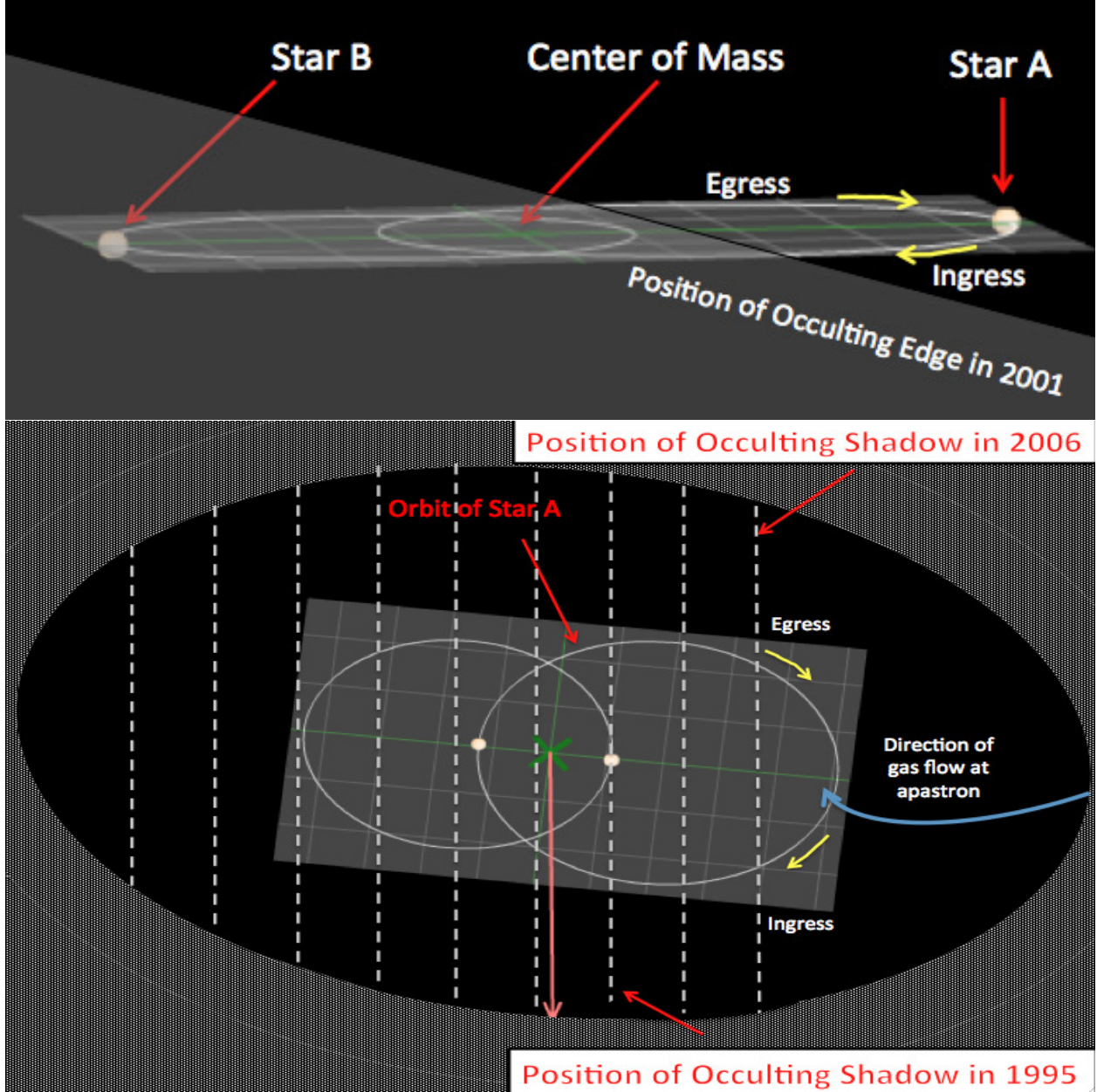


Fig. 1.— The top panel depicts the KH 15D system roughly edge on with the stars positioned at apastron. The bottom panel shows a top view of the system with the stars positioned at periastron. The pink arrow denotes the direction to Earth. The blue arrow to the right of the figure shows the inferred direction of the gas flow, as discussed in §4. This figure was created with the help of an eclipsing binary simulator produced by the University of Nebraska-Lincoln, freely available at <http://astro.unl.edu/>.

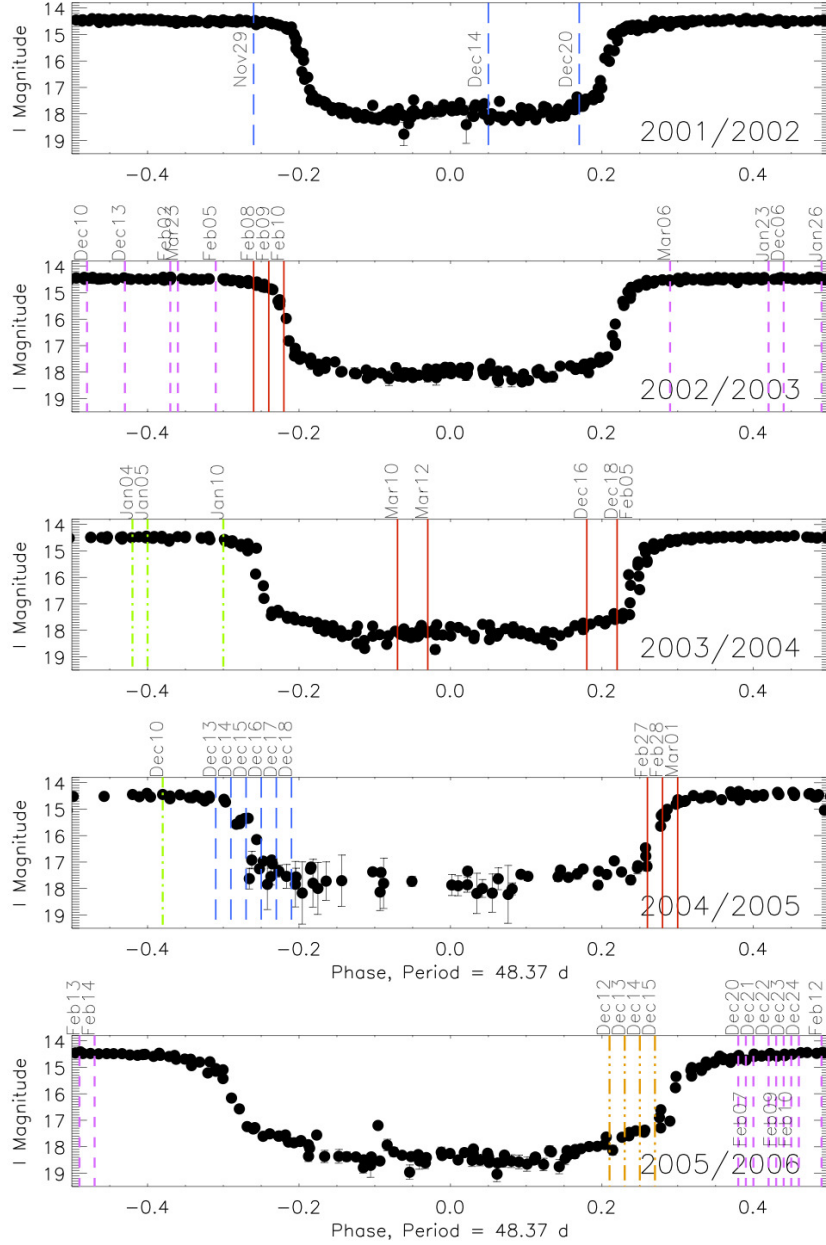


Fig. 2.— Phases at which high-resolution spectra were obtained. Solid red lines represent data obtained with the Keck I telescope and HIRES. Long dashed blue lines represent data obtained with the VLT and UVES. Pink dashed lines represent data obtained with the HET and the HRS. Green dash-dot lines represent data obtained at the McDonald Observatory 2.1-m telescope and the Sandiford Cassegrain Echelle spectrograph. Orange dash-dot-dot-dot lines represent data obtained with the Magellan Clay telescope and the MIKE spectrometer.

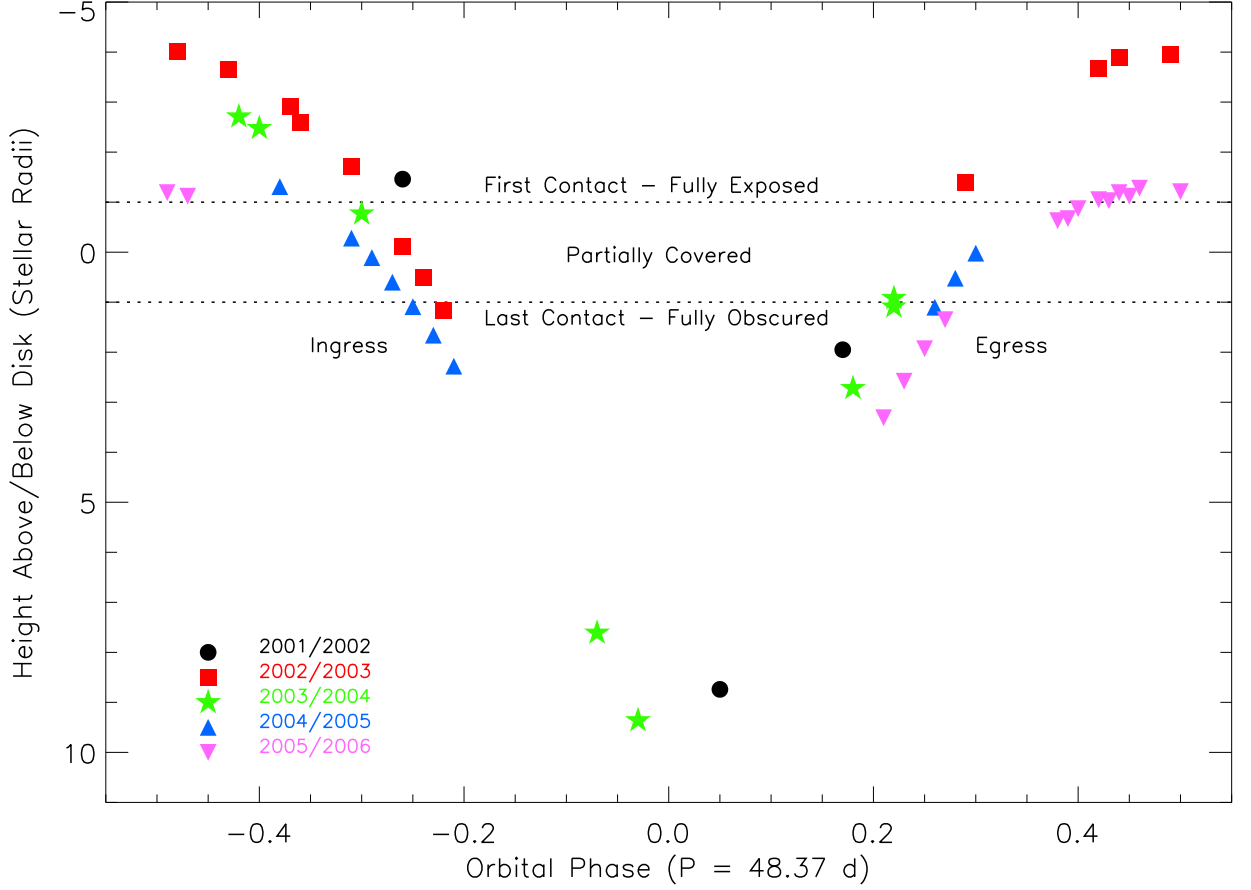


Fig. 3.— Predicted height from W06 of star A above the occulting screen in stellar radii versus phase over the course of five different observing seasons. Note that the same phase does not correspond to the same height above or below the disk due to the precession of the circumbinary ring. The dotted lines in the figure represent the points at which the star makes first and last contact with the edge of the disk from our point of view.



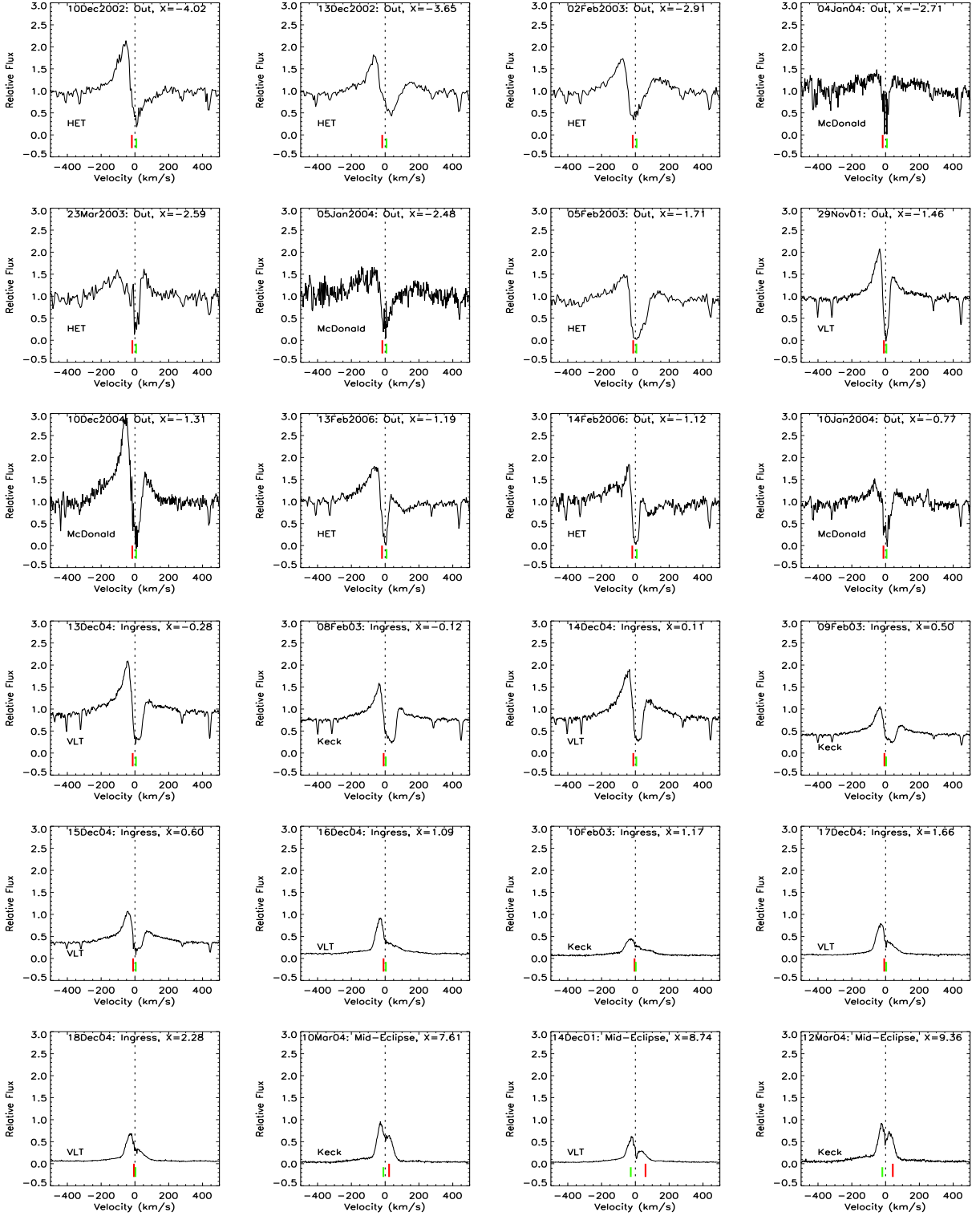


Fig. 4.— From left to right, H $\alpha$  emission line profiles out-of-eclipse through ingress to mid-eclipse. The red (long) and green (short) tickmarks represent the predicted velocities of stars A and B, respectively. All profiles are shown in the reference frame of the system.

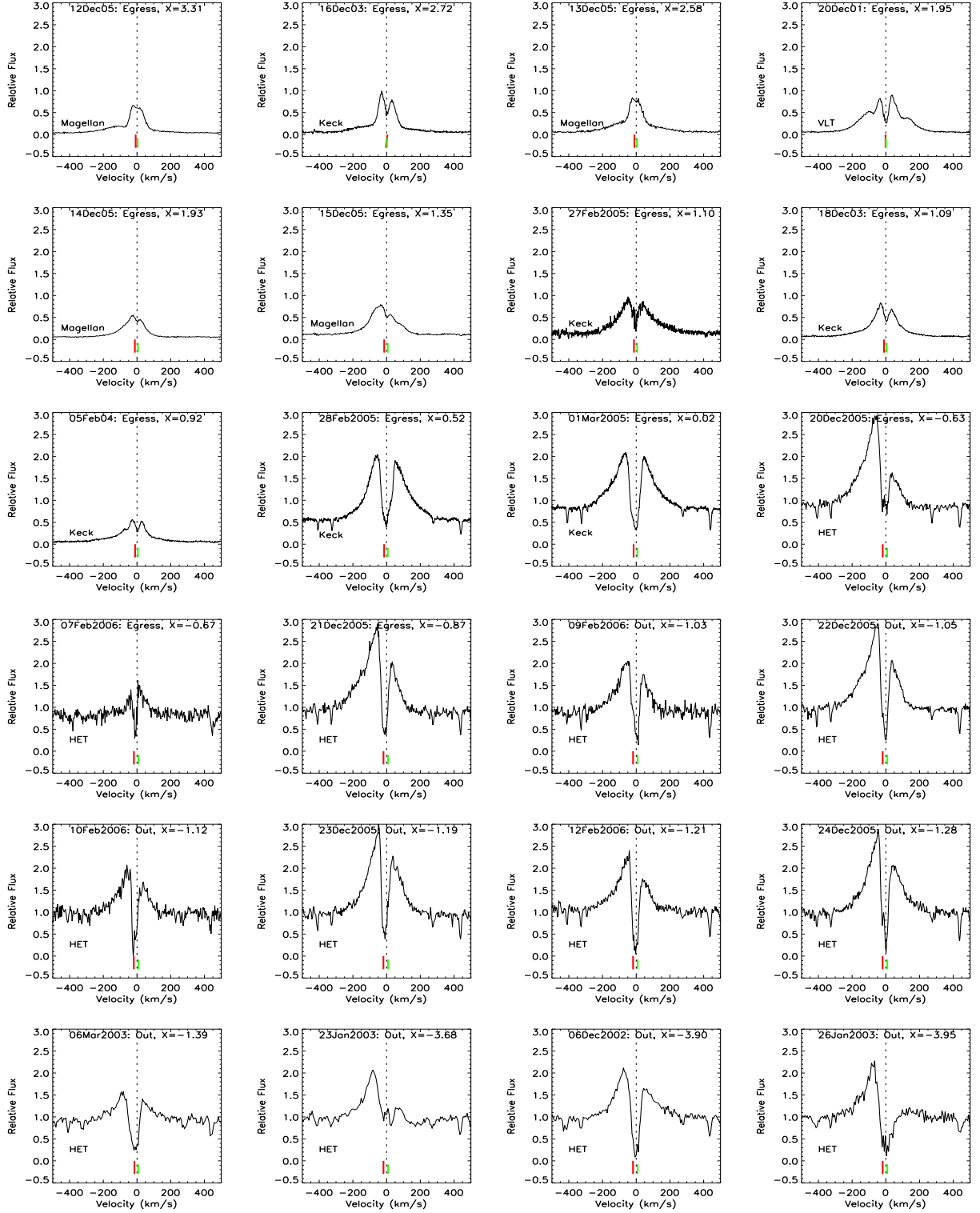


Fig. 5.— Left to right, top to bottom, H $\alpha$  emission line profiles are shown during egress and ending out-of-eclipse. The red (long) and green (short) tickmarks indicate the radial velocities of star A and B, respectively. All profiles are shown in the reference frame of the system.

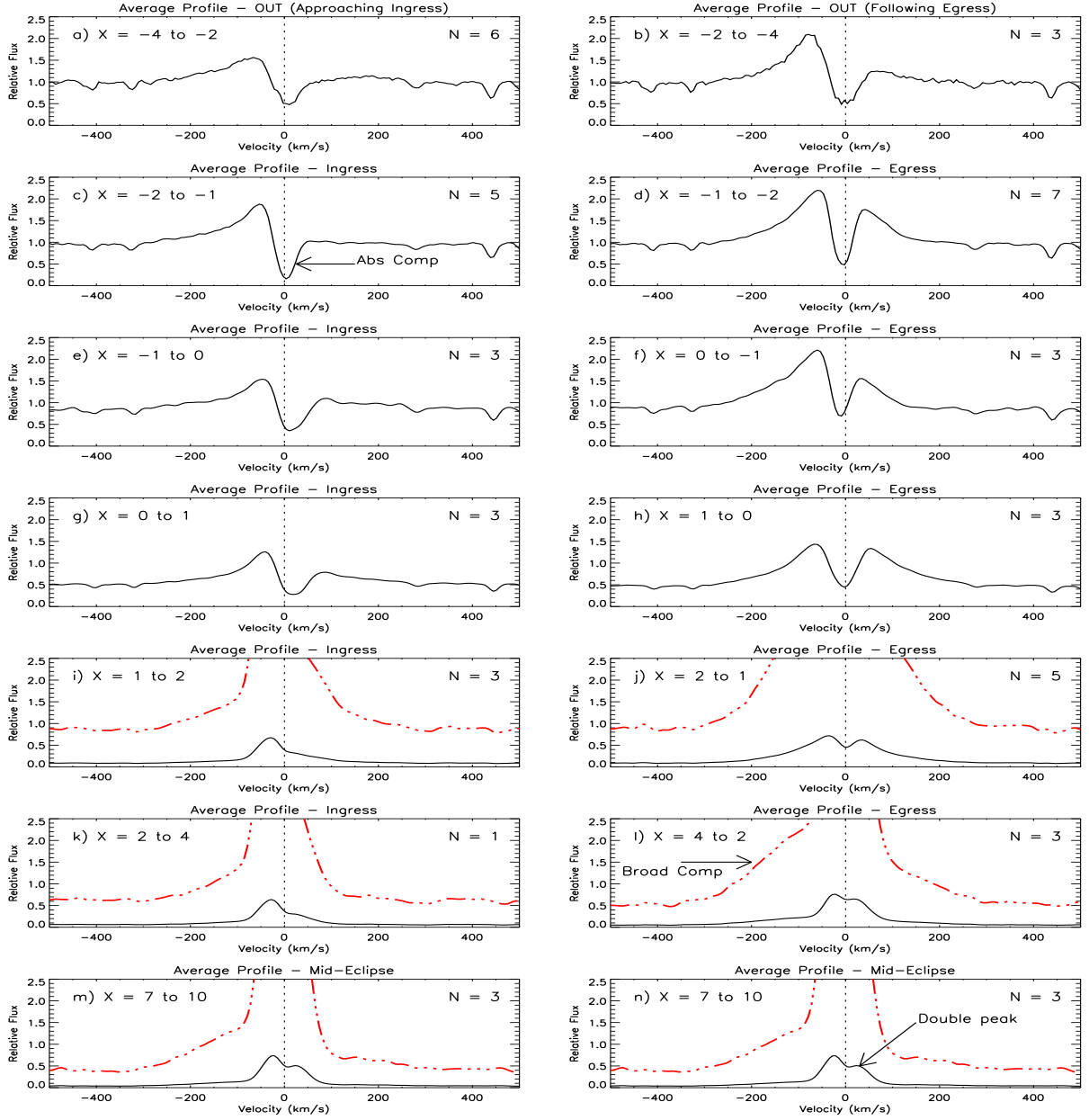


Fig. 6.— The profiles from Figures 4 and 5 averaged according their distances above or below the occulting disk. The letter  $N$  in the upper right hand corner designates how many spectra went into creating the average. The bottom two panels are identical and represent mid-eclipse. Hence, the panels on the left side of the figure represent ingress, while the panels on the right side of the figure represent egress. The red dash-dot-dot-dot profile shown in the bottom six panels is the average profile for that distance bin multiplied by 10 to show more clearly the blue wing present after the star is fully eclipsed.

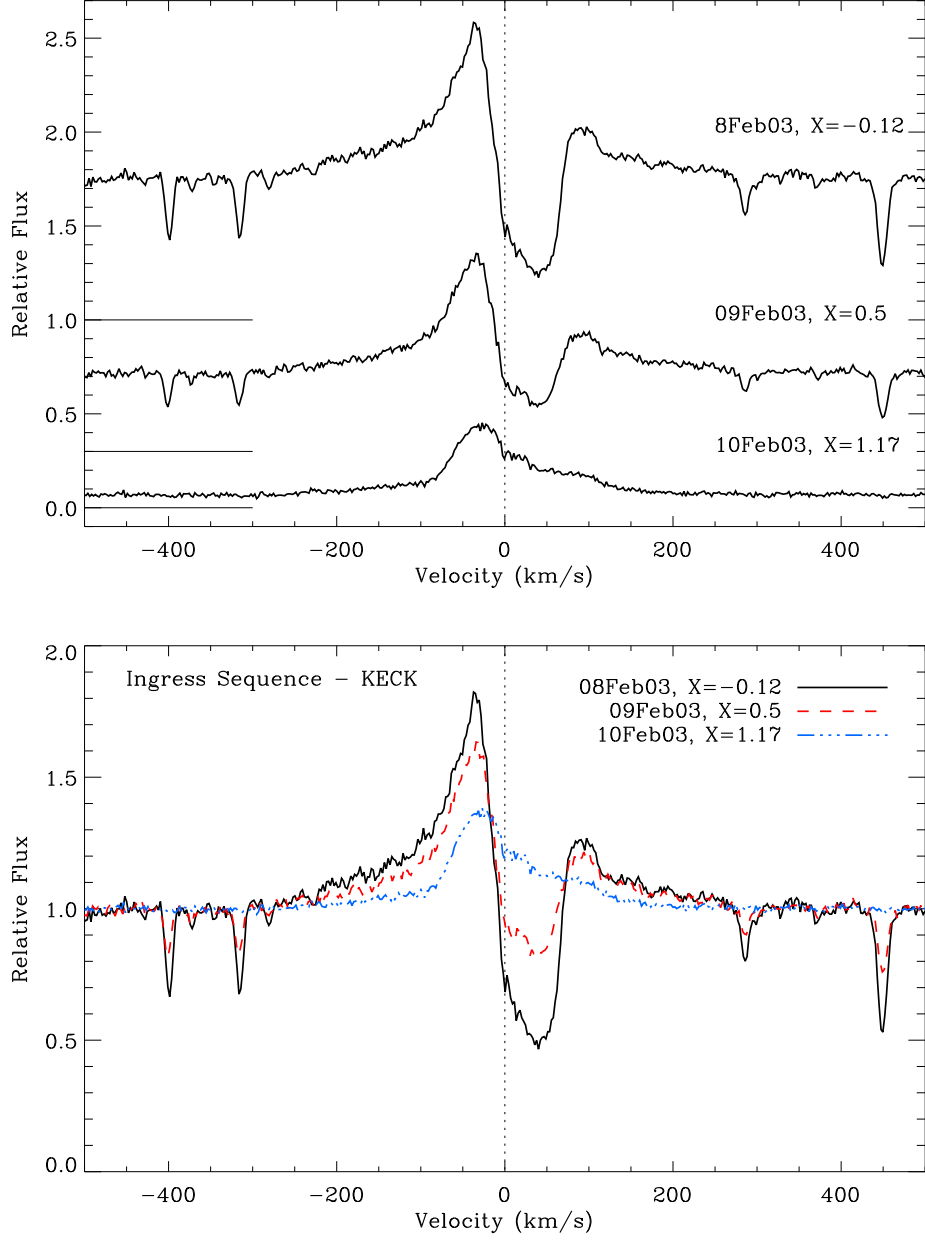


Fig. 7.— The top panel shows a 3 day sequence of spectra obtained at Keck during an ingress in 2003 February. Each spectrum has an offset applied, with the zero point indicated by a small horizontal line along the y-axis. The bottom panel shows the spectra appropriately fluxed and normalized to 1.0 so that each spectrum can be plotted on top of one another.

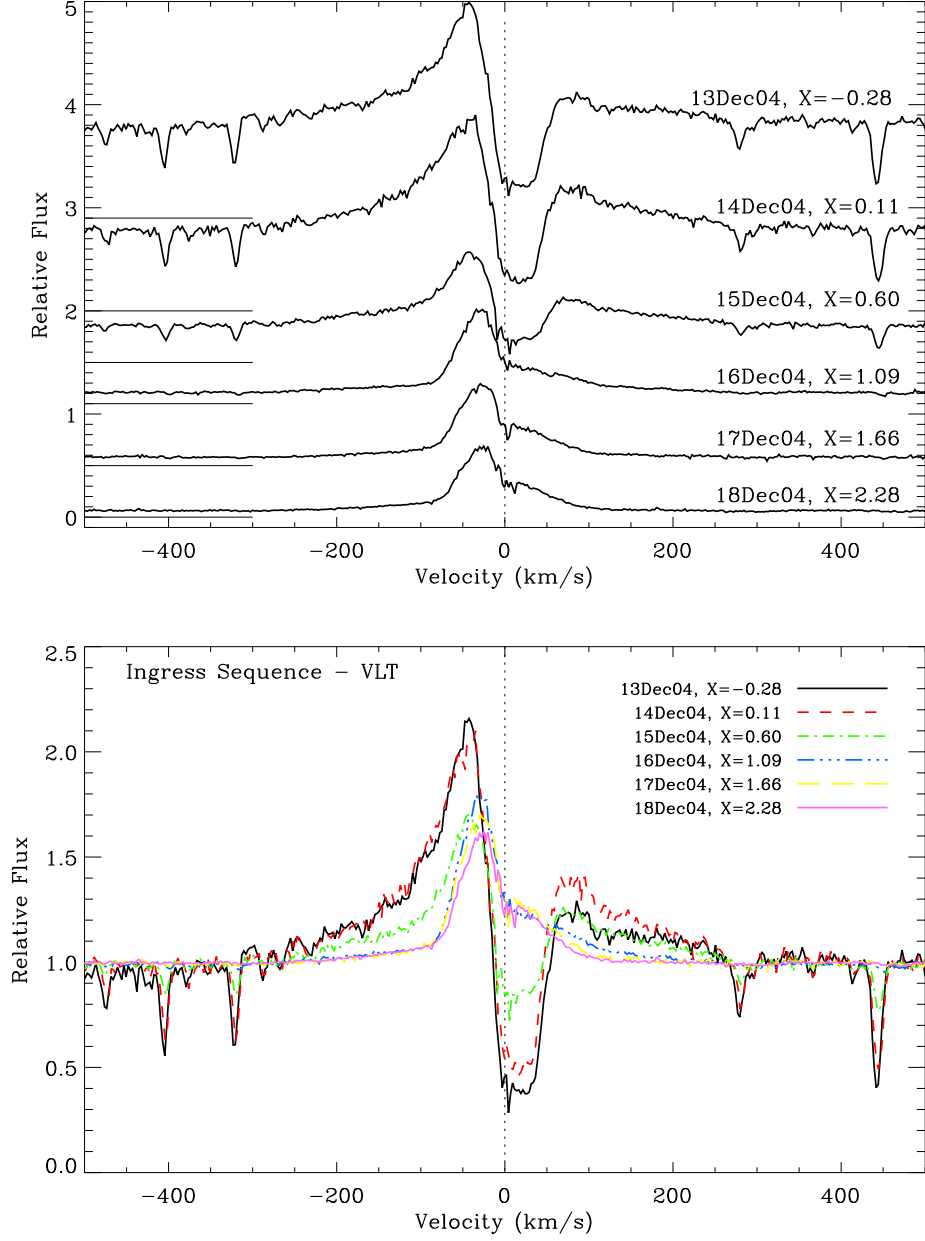


Fig. 8.— The top panel shows a 6 day sequence of spectra obtained at the VLT during an ingress in 2004 December. Each spectrum has an offset applied, with the zero point indicated by a small horizontal line along the y-axis. The bottom panel shows the spectra appropriately fluxed and normalized to 1.0 so that each spectrum can be plotted on top of one another.

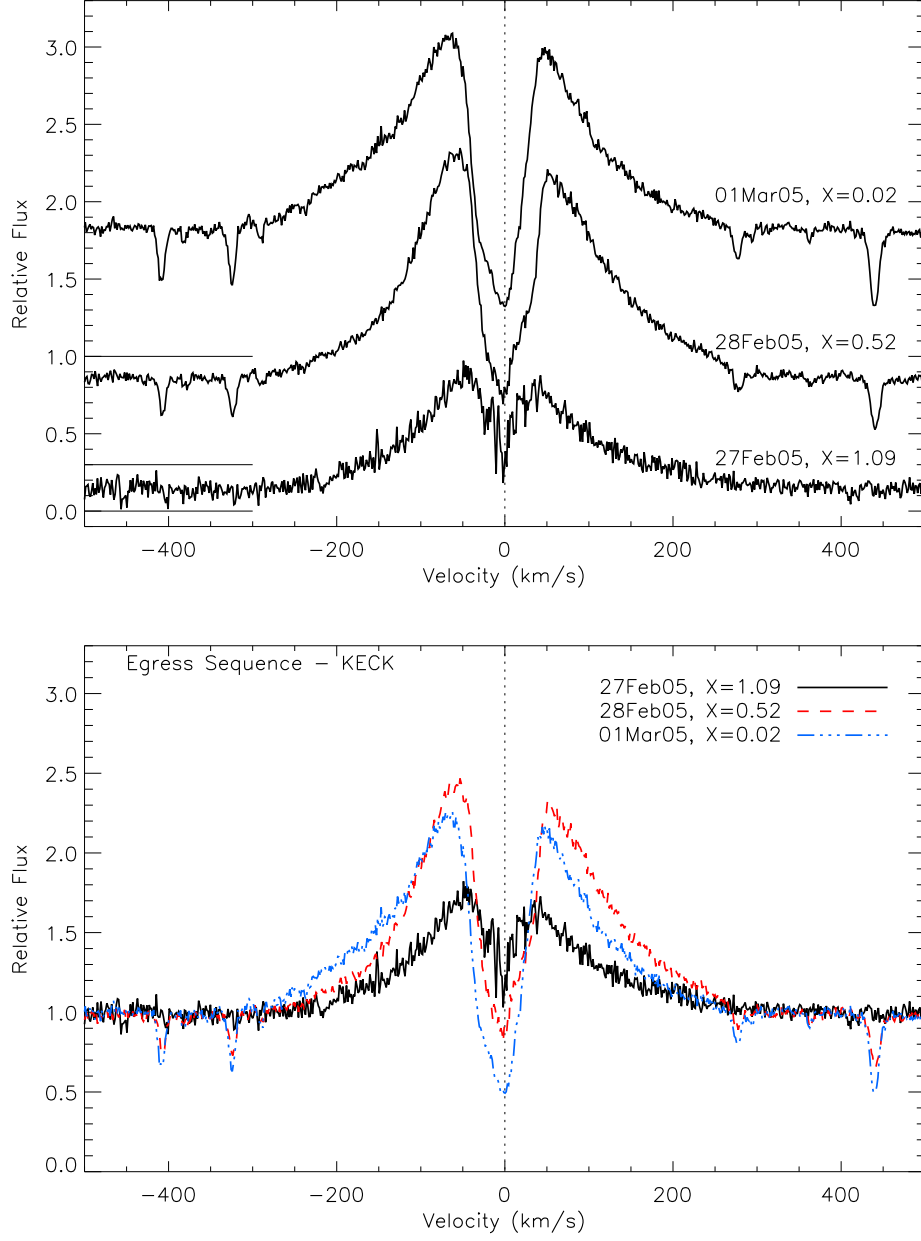


Fig. 9.— The top panel shows three spectra obtained during egress. Each spectrum has an offset applied, with the zero point indicated by a small horizontal line along y-axis. The bottom panel shows the spectra appropriately fluxed and normalized to 1.0 so that each spectrum can be plotted on top of one another.

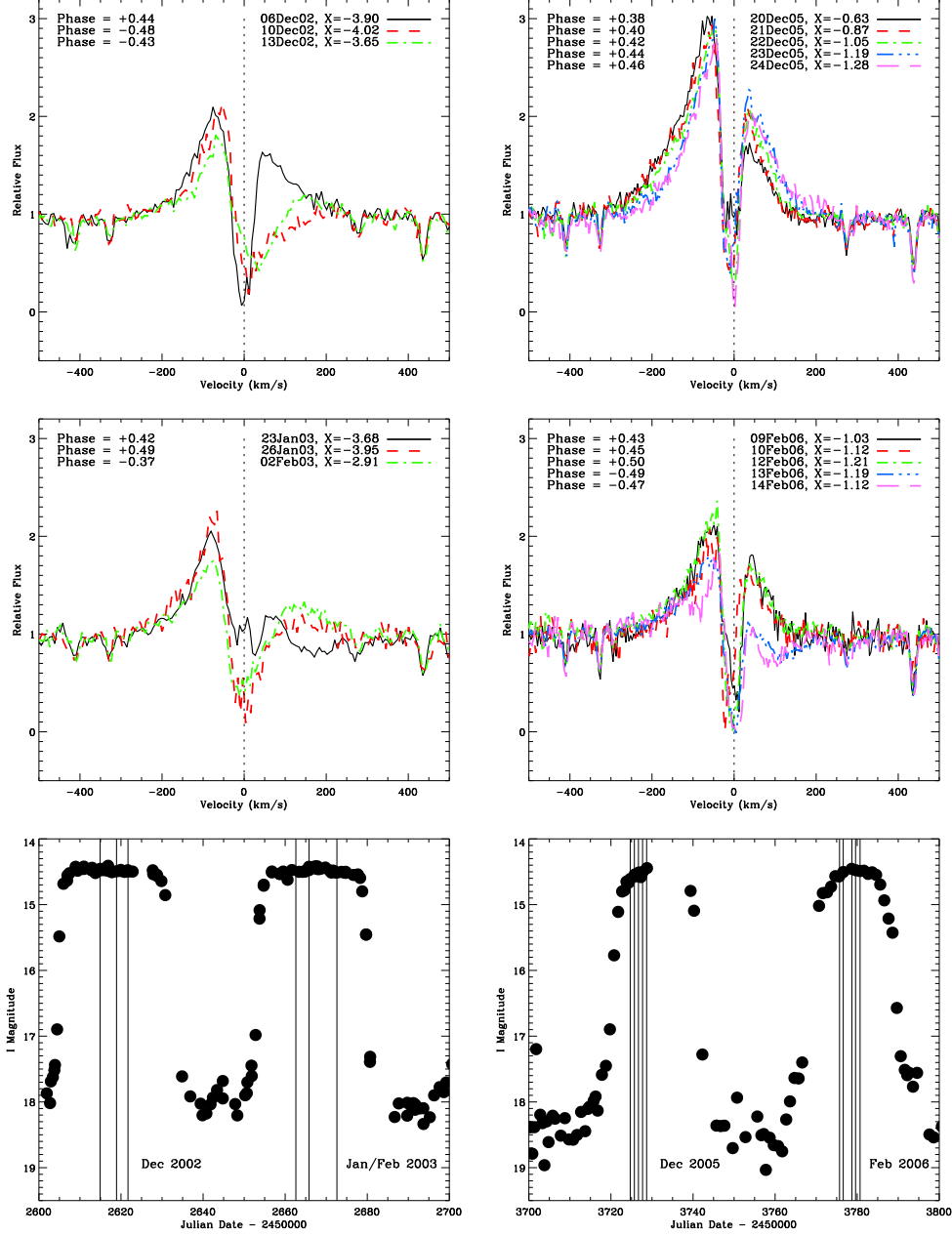


Fig. 10.— H $\alpha$  profiles obtained while star A is the farthest out of eclipse. The three left panels represent data taken during the 2002/2003 observing season. The three panels on the right show data obtained during the 2005/2006 observing season.

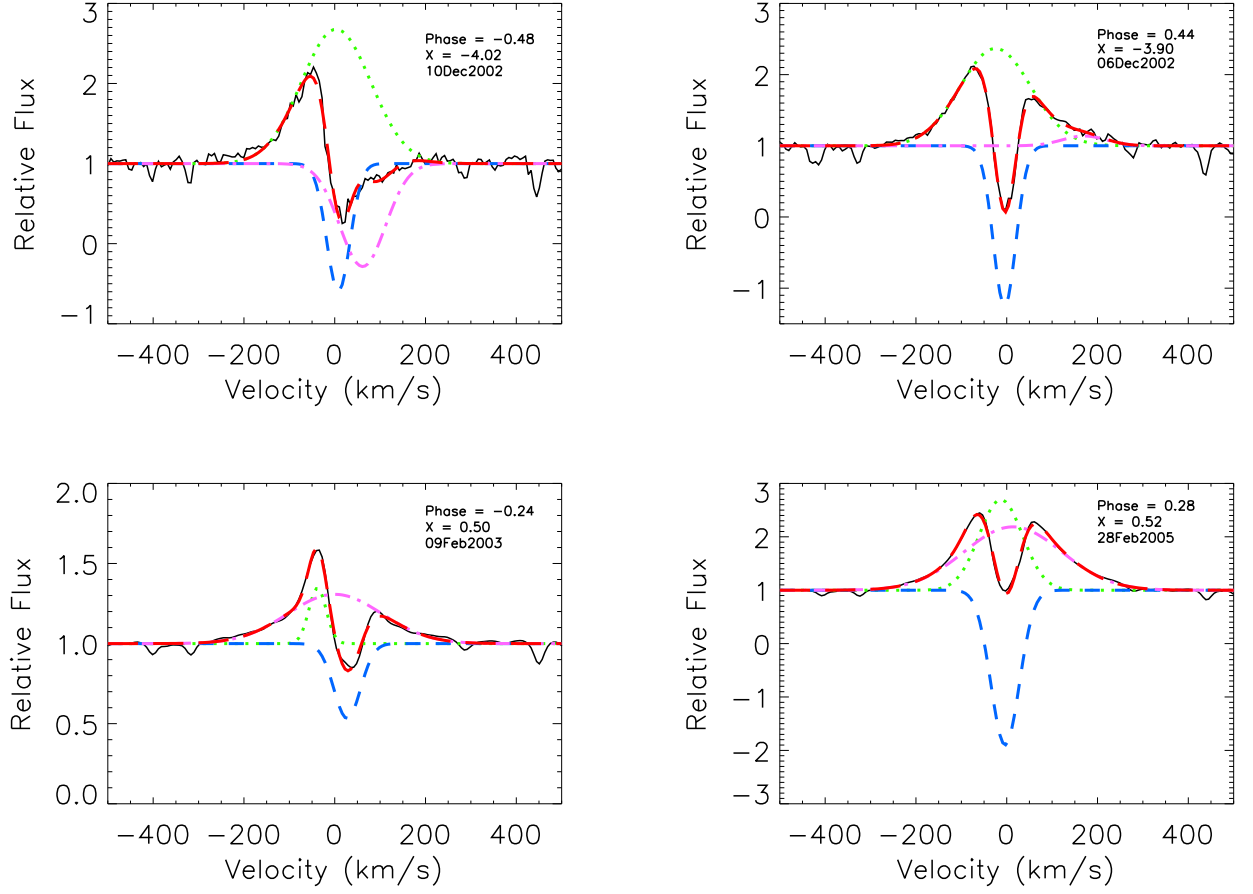


Fig. 11.— Sample of profiles and three gaussian fits. The combined fit is shown in red.



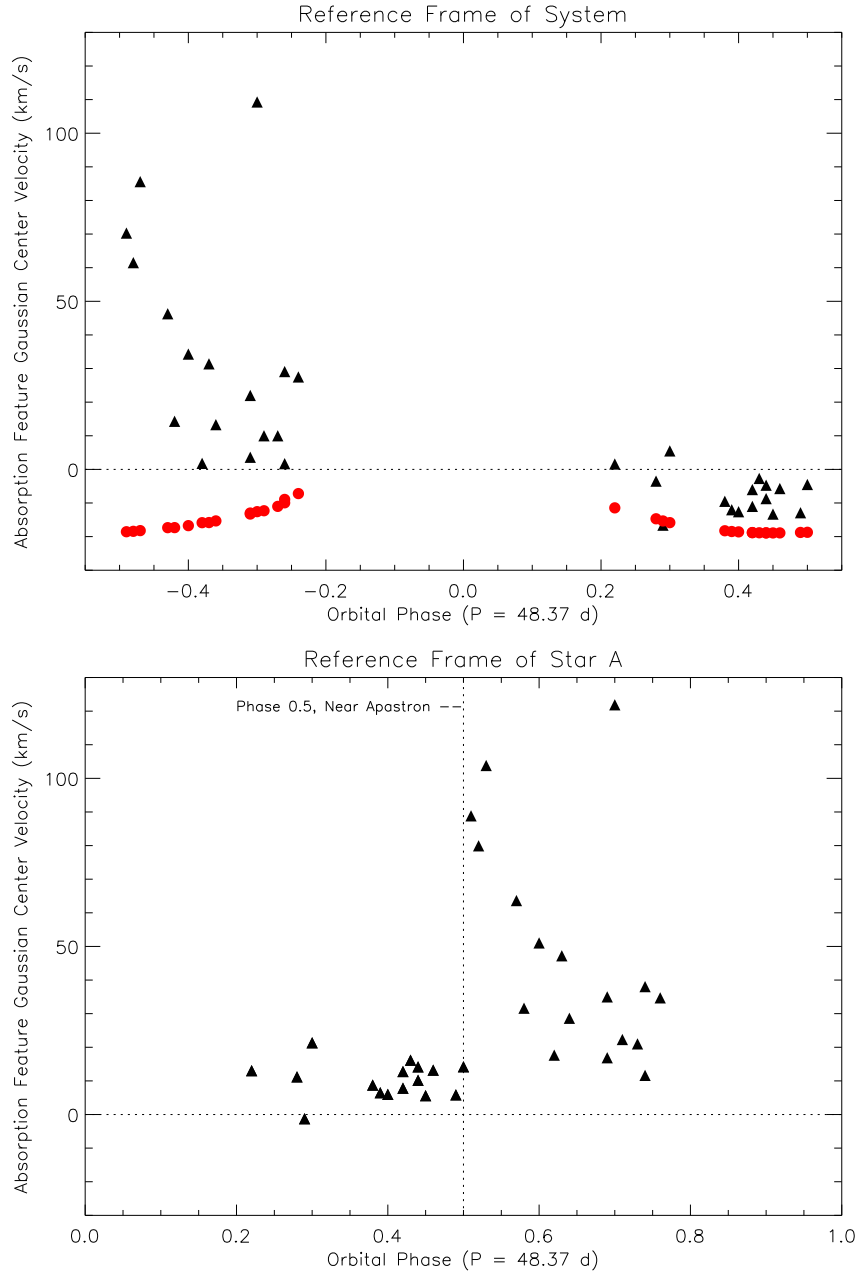


Fig. 12.— The black triangles represent the velocity center of the gaussian fit to the absorption component of the observed profiles. Plotted in red are the predicted velocities of Star A for each observation. The horizontal dotted line represents the rest frame of the system. The bottom panel shows the velocity of the absorption component versus phase in the reference frame of star A as viewed from the Earth, and the horizontal dotted line represents the rest frame of the star.

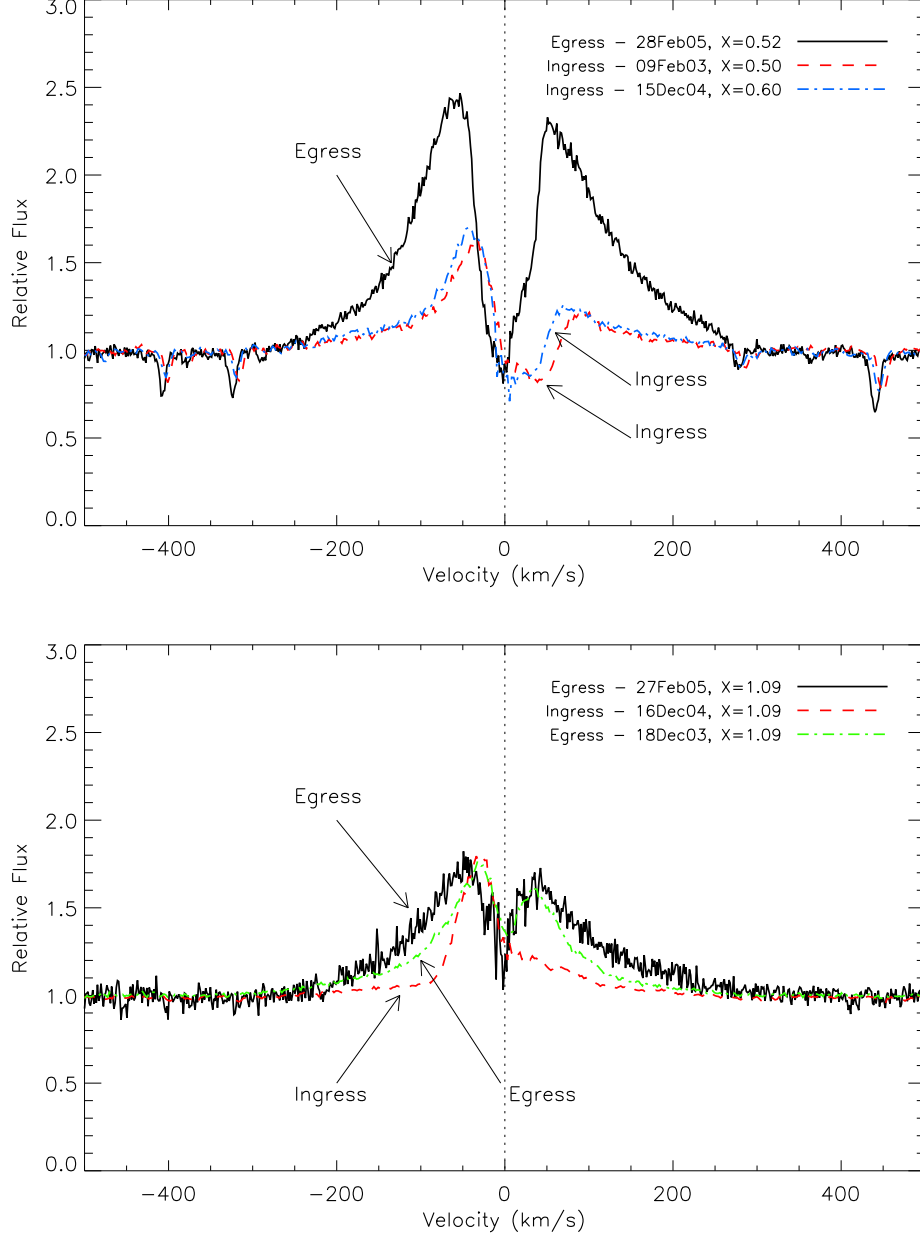


Fig. 13.— The top panel shows a comparison of ingress and egress spectra when the star was at a distance below the CBD edge of  $\Delta X \sim 0.5$ . The bottom panel shows the same comparison, but for spectra taken when the star was at the edge of the CBD but still occulted.

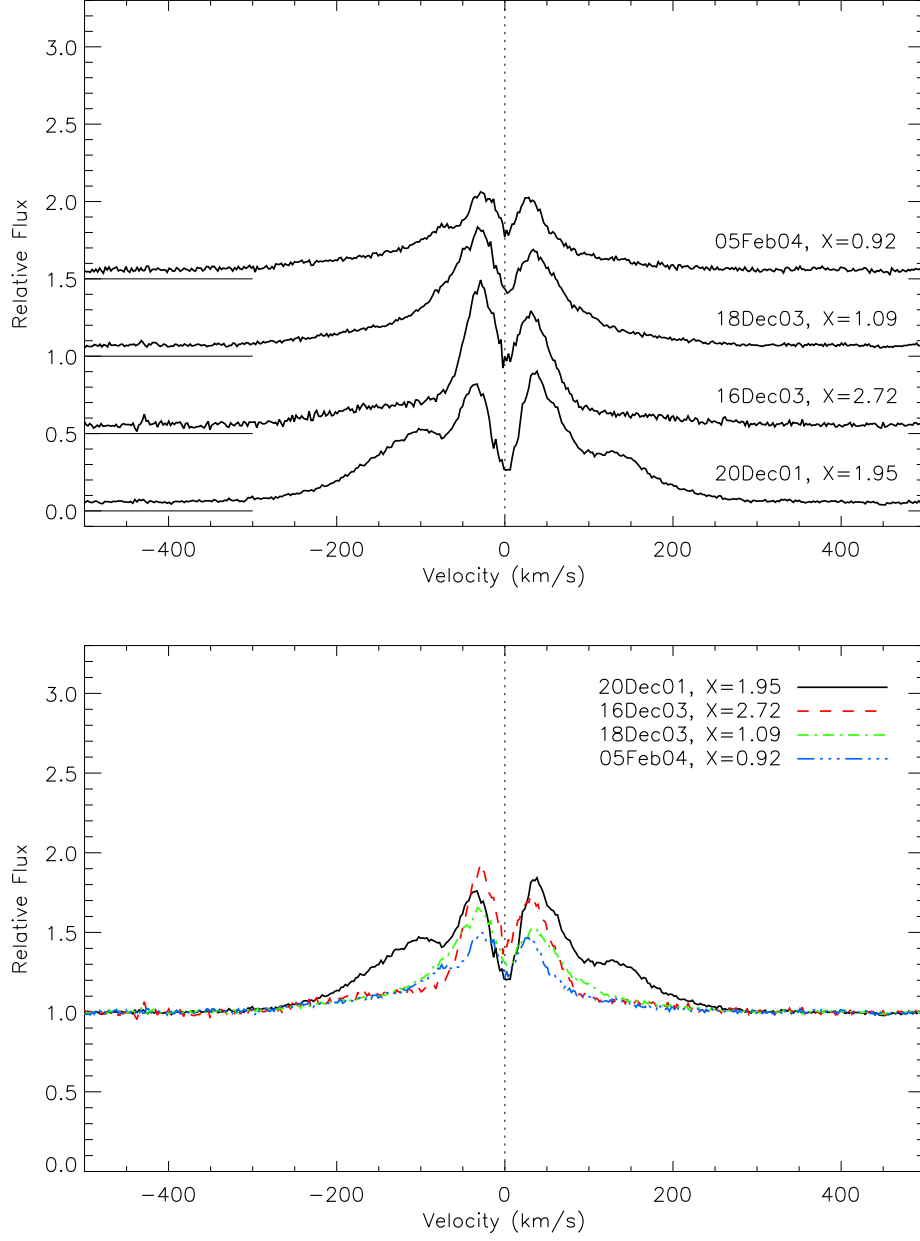


Fig. 14.— The top panel shows 4 spectra obtained during various egresses over the course of 2 observing seasons (2001/2001, 2002/2003). Each spectrum has an offset applied, with the zero point indicated by a small horizontal line along the y-axis. The bottom panel shows the spectra appropriately fluxed and normalized to 1.0 so that each spectrum can be plotted on top of one another.

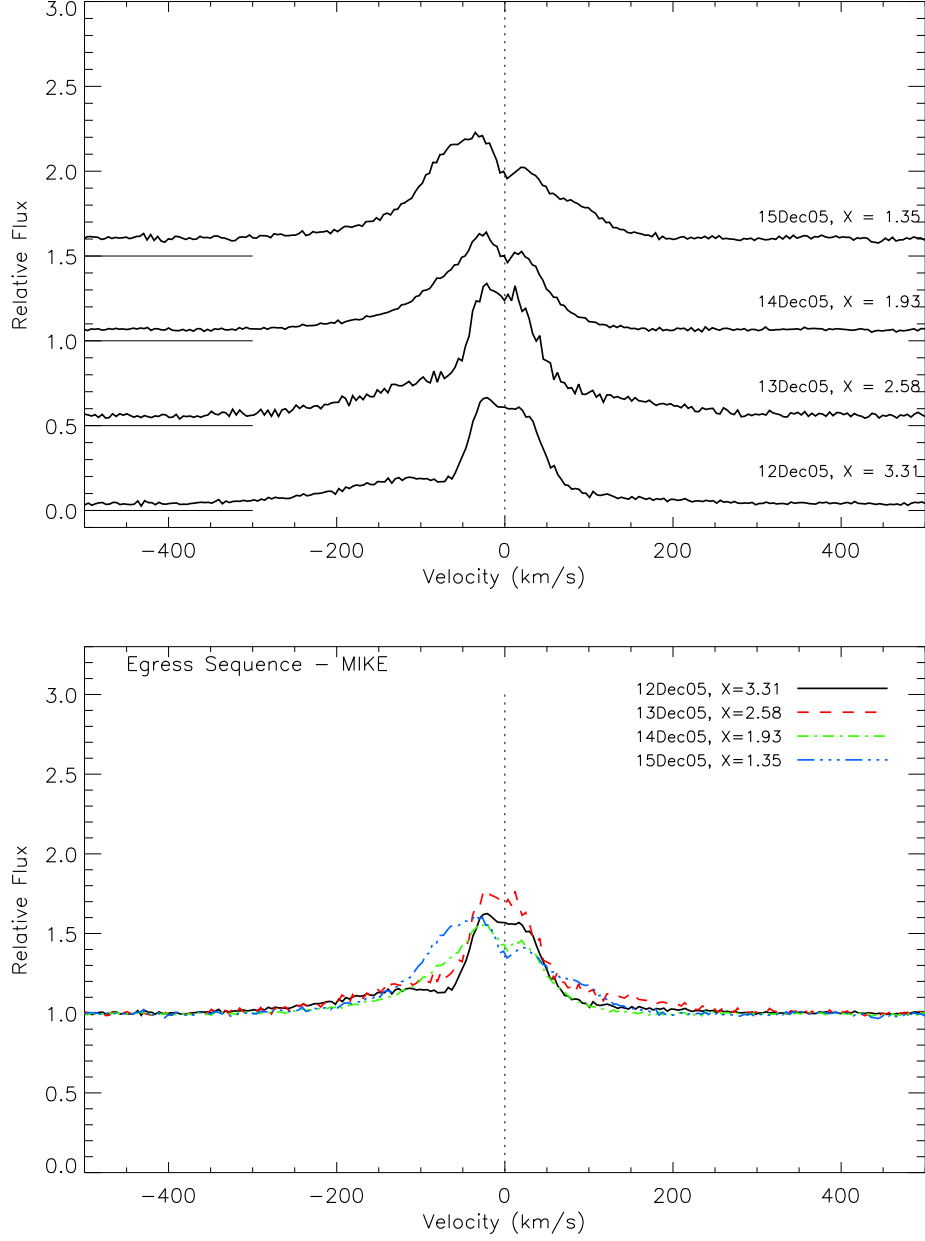


Fig. 15.— The top panel shows 4 spectra obtained on consecutive nights during an egress that took place in 2005 December. Each spectrum has an offset applied, with the zero point indicated by a small horizontal line along the y-axis. The bottom panel shows the spectra appropriately fluxed and normalized to 1.0 so that each spectrum can be plotted on top of one another.

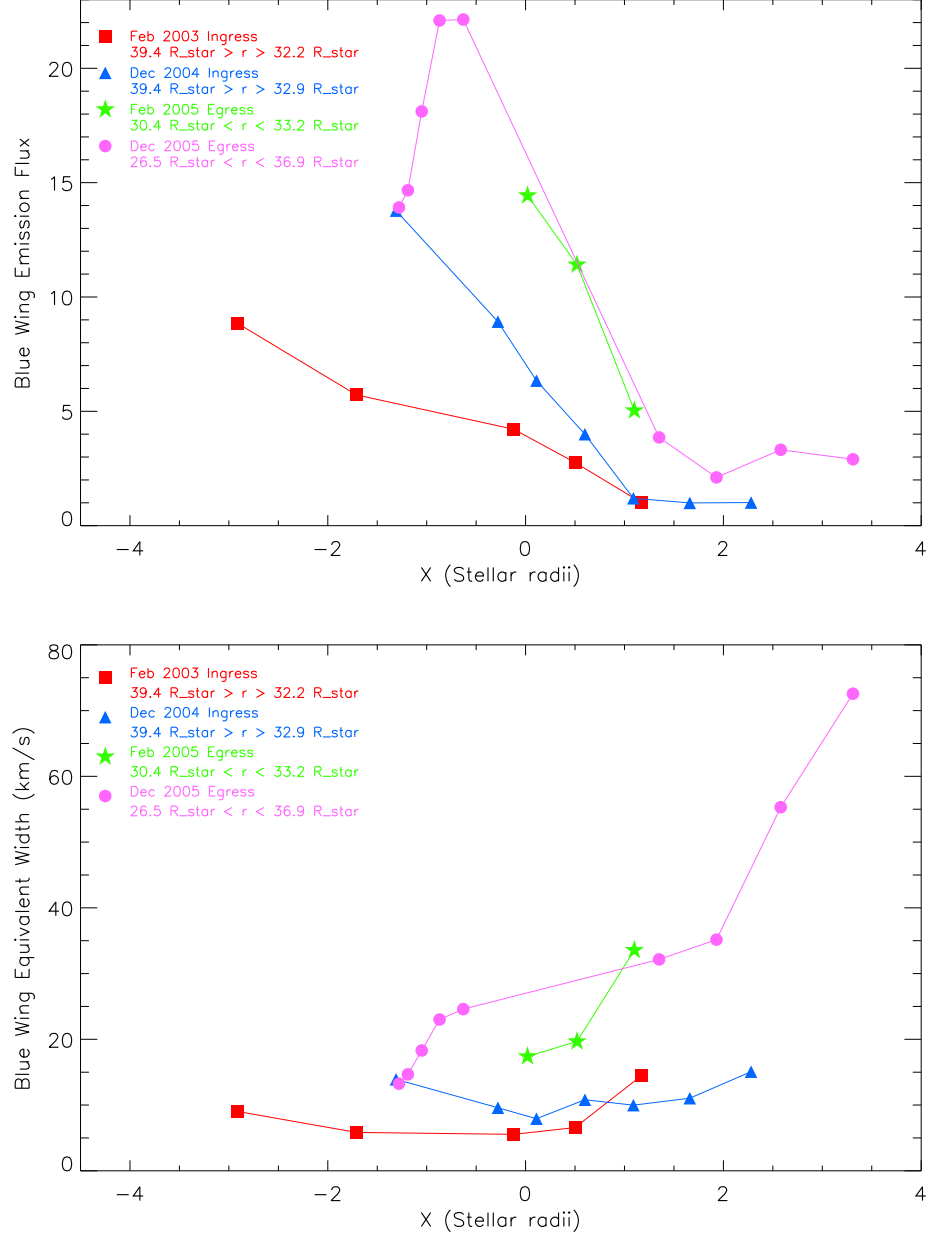


Fig. 16.— The top panel shows the blue wing emission flux between  $-85$  and  $-280$   $\text{km s}^{-1}$  measured for star A as it undergoes various ingress/egress events as noted in the figure. The bottom panel shows the equivalent width of the blue wing between  $-85$  and  $-280$   $\text{km s}^{-1}$  for the same set of ingress/egress events.

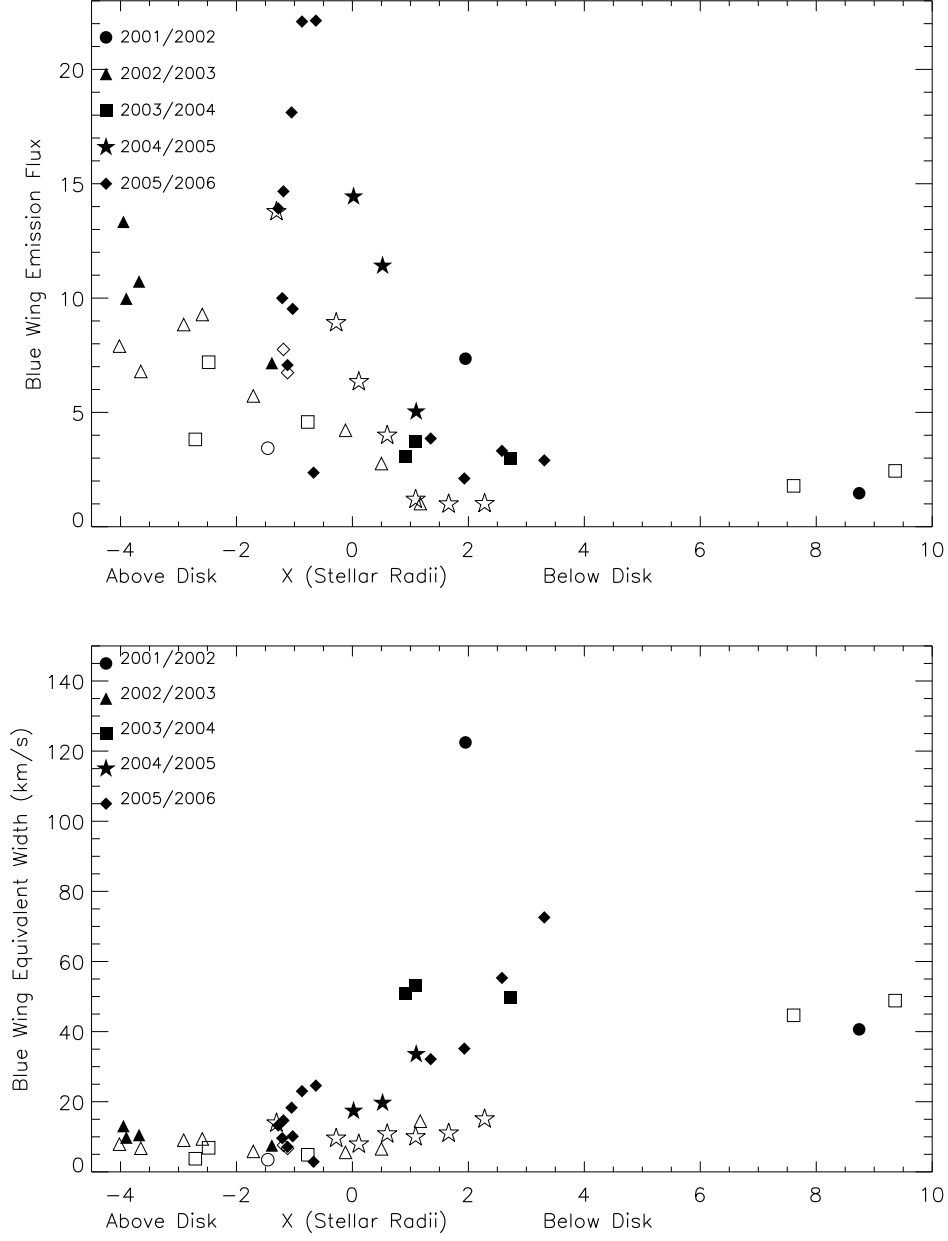


Fig. 17.— The top panel shows the blue wing emission flux between  $-85$  and  $-280$   $\text{km s}^{-1}$  measured for star A for all 48 observations. The bottom panel shows the equivalent width of the blue wing between  $-85$  and  $-280$   $\text{km s}^{-1}$  for the same set of observations.

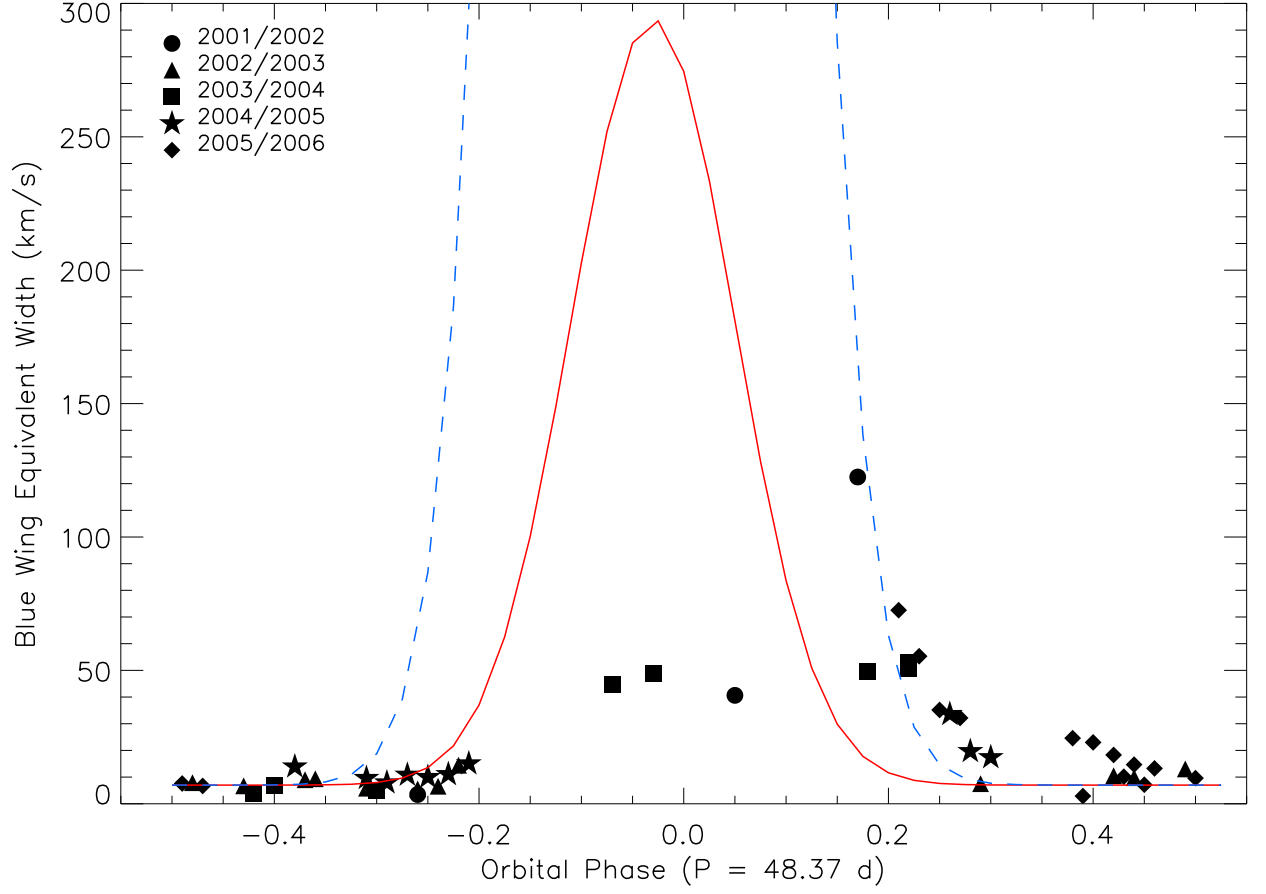


Fig. 18.— The EW of the  $H\alpha$  emission between  $-85$  and  $-280 \text{ km s}^{-1}$ . The solid red line represents a gaussian fit to match the gas accretion rate from Figure 2 of Artymowicz & Lubow (1996). The dashed blue line is the same gaussian scaled to match the egress EW.